



Pacific Northwest
NATIONAL LABORATORY

Proudly Operated by Battelle Since 1965

Process Modeling of U-10wt% Mo Alloys Using Integrated Computational Materials Engineering

March 2019

C Wang
A Soulami
Z Xu
G Cheng
S Hu
D Burkes

WE Frazier
KS Choi
X Wang
X Hu
CA Lavender
VV Joshi

DISCLAIMER

This report was prepared as an account of work sponsored by an agency of the United States Government. Neither the United States Government nor any agency thereof, nor Battelle Memorial Institute, nor any of their employees, **makes any warranty, express or implied, or assumes any legal liability or responsibility for the accuracy, completeness, or usefulness of any information, apparatus, product, or process disclosed, or represents that its use would not infringe privately owned rights.** Reference herein to any specific commercial product, process, or service by trade name, trademark, manufacturer, or otherwise does not necessarily constitute or imply its endorsement, recommendation, or favoring by the United States Government or any agency thereof, or Battelle Memorial Institute. The views and opinions of authors expressed herein do not necessarily state or reflect those of the United States Government or any agency thereof.

PACIFIC NORTHWEST NATIONAL LABORATORY
operated by
BATTELLE
for the
UNITED STATES DEPARTMENT OF ENERGY
under Contract DE-AC05-76RL01830

Printed in the United States of America

Available to DOE and DOE contractors from
the Office of Scientific and Technical
Information,
P.O. Box 62, Oak Ridge, TN 37831-0062
www.osti.gov
ph: (865) 576-8401
fox: (865) 576-5728
email: reports@osti.gov

Available to the public from the National Technical Information Service
5301 Shawnee Rd., Alexandria, VA 22312
ph: (800) 553-NTIS (6847)
or (703) 605-6000
email: info@ntis.gov
Online ordering: <http://www.ntis.gov>

Process Modeling of U-10wt% Mo Alloys Using Integrated Computational Materials Engineering

C Wang

A Soulami

Z Xu

G Cheng

S Hu

D Burkes

WE Frazier

KS Choi

X Wang

X Hu

CA Lavender

VV Joshi

March 2019

Prepared for
the U.S. Department of Energy
under Contract DE-AC05-76RL01830

Pacific Northwest National Laboratory
Richland, Washington 99352

Summary

Low-enriched uranium alloyed with 10 wt% molybdenum (U-10Mo) has been identified as a promising alternative to highly enriched uranium as fuel for the nation's high-performance research reactors. Manufacturing the U-10Mo alloy consists of multiple complex thermomechanical processes, which is highly challenging for computational modeling. The integrated computational materials engineering (ICME) concept supports building a microstructure-based framework to investigate the effect of manufacturing processes on the material microstructure. In this report, an ICME model that combines homogenization, hot rolling, annealing, and cold rolling is presented as an example of implementing the ICME concept for modeling the manufacturing processes of the U-10Mo alloy. The integrated model enables information to be passed between the different model components, leading to an improved prediction and a better understanding of microstructure across multiple processes. The integrated model was also implemented to investigate the variation of chemical composition, thickness of the zirconium interlayer, grain growth, and carbide redistribution and fracture of U-10Mo during the thermomechanical processes. With the homogenization model, a molybdenum concentration map can be reconstructed from any given microstructure, and the homogenization time needed to reach a desired homogenization level can also be approximated. The microstructure-based finite-element rolling model, shows that the homogenization process reduces the nonuniformity in the thickness of the zirconium interlayers on the U-10Mo. With the output from the rolling model, a statistical analysis of second-phase hard particles was conducted to quantify the particle redistribution and interparticle spacing between carbides during the deformation. Also, new stringer identification criteria were proposed to predict the correlation between stringer volume fractions and hot-rolling reduction. A macro-finite-element method hot-rolling model showed that higher reduction passes can be achieved within the mill separation force range, and a new "aggressive" rolling schedule was proposed. The model also showed the importance of can material on the quality of rolled foils, with stronger can materials resulting in hot-rolled U-10Mo free of defects (waviness, dog-boning). The deformation-induced recrystallization model demonstrated capability to use inputs from deformation simulations of strain accumulation in U-10Mo samples to predict grain growth behavior of the fuel during thermal treatment stages. Finally, a plane-strain compression mode simulated particle fracture and calculates the void volume fraction generated during cold rolling. The macro-finite-element method cold-rolling model showed that smaller diameter rolls are necessary to achieve the desired foil thickness.

Acknowledgments

The current work was supported by the U.S. Department of Energy's National Nuclear Security Administration. Pacific Northwest National Laboratory is operated by Battelle for the U.S. Department of Energy under Contract DE-AC05-76RL01830. The authors would like to acknowledge Dr. Dongsheng Li for his preliminary input to this work. The authors also would like to thank Crystal Rutherford, Anthony Guzman, Danny Edwards, and Alan Schemer-Kohn, all of Pacific Northwest National Laboratory, for assisting in the microstructural characterization, as well as all other staff directly or indirectly associated with producing the results. The authors also thank Mr. Glenn Moore, Mr. Brady Mackowiak, Mr. Steve Steffler, and Mr. Jason Schulthess, all of Idaho National Laboratory, for fabrication and supply of the U-10Mo test samples.

Acronyms and Abbreviations

°C	degrees Celsius
BSE	backscattered electron
BWXT	BWX Technologies, Inc.
EBSD	electron backscatter diffraction
EDS	energy dispersive spectroscopy
FEA	finite-element analysis
FEM	finite-element method
HIP	hot isostatic pressing
ICME	integrated computational materials engineering
LEU	low-enriched uranium
Mo	molybdenum
PNNL	Pacific Northwest National Laboratory
PVF	particle volume fraction
RVE	representative volume element
SEM	scanning electron microscopy
SVF	stringer volume fraction
TI	tolerance interval
U-10Mo	uranium alloy with ten weight percent molybdenum (22 atomic percent Mo)
UC	uranium carbide
U-Mo	uranium-molybdenum
UTS	ultimate tensile strength
wt%	weight percent
Zr	zirconium

Contents

Summary	iii
Acknowledgments.....	v
Acronyms and Abbreviations	vii
Contents	ix
Figures	xi
Tables.....	xii
1.0 Introduction	1.1
2.0 Homogenization.....	2.1
2.1 Model Description.....	2.1
2.2 Model Validation.....	2.2
2.3 Impact for the Program	2.3
2.4 Tools Developed	2.5
2.4.1 Determine Sample Qualification.....	2.5
2.4.2 Determine Homogenization Time and Temperature.....	2.7
3.0 Hot Rolling	3.1
3.1 Macro-FEM Model	3.1
3.1.1 Model Description.....	3.1
3.1.2 Model Validation.....	3.1
3.1.3 Impact for Program	3.2
3.1.4 Tools Developed	3.4
3.2 Microstructure-Based FEM Model	3.4
3.2.1 Model Description.....	3.5
3.2.2 Model Validation.....	3.7
3.2.3 Impact for Program	3.7
3.2.4 Tools Developed	3.10
4.0 Annealing	4.1
4.1 Model Description.....	4.1
4.1.1 Integration with FEM Rolling Model.....	4.1
4.2 Model Validation.....	4.2
4.3 Impact for Program	4.5
4.4 Tools Developed	4.6
5.0 Cold Rolling	5.1
5.1 Macro-FEM Model	5.1
5.1.1 Model Description.....	5.1
5.1.2 Model Validation.....	5.1
5.1.3 Impact for Program	5.1

5.1.4	Tools Developed	5.4
5.2	Microstructure-Based FEM Model	5.4
5.2.1	Model Description.....	5.4
5.2.2	Model Validation.....	5.5
5.2.3	Impact for Program	5.6
5.2.4	Tools Developed	5.6
6.0	Post-Cold-Rolling Recrystallization.....	6.1
6.1	Model Description.....	6.1
6.2	Model Validation.....	6.2
6.3	Impact for Program	6.2
6.4	Tools Developed	6.2
7.0	Post-Recrystallization Grain Growth.....	7.1
7.1	Model Description.....	7.1
7.2	Model Validation.....	7.3
7.3	Impact for Program	7.4
7.4	Tools Developed	7.4
8.0	Integration Framework	8.1
9.0	References	9.1

Figures

Figure 1.1. Inputs and Outputs of the Integrated Model for U-10Mo Processing	1.3
Figure 1.2. Integrated Model for Material Processing of U-10Mo	1.4
Figure 2.1. Images of As-Cast U-10Mo.....	2.1
Figure 2.2. Homogenization Kinetics from Simulation (line) and Experimental BSE-SEM Images.....	2.2
Figure 2.3. BSE-SEM Images, Mo Atomic Concentration along the EDS Lines, and the Reconstructed Mo Concentrations for Top, Middle and Bottom Sections of Y-12 LEU-Mo Sample	2.4
Figure 2.4. Simulated Homogenization Kinetics for A3-90 and Y-12 LEU-Mo Samples	2.5
Figure 2.5. Relationship of k_2 and its Gradient to N	2.6
Figure 3.1. Measured Separation Forces Compared to Simulated Separation Forces	3.2
Figure 3.2. Thickness Variation Across the Length of the U-10Mo Coupon	3.3
Figure 3.3. Representation of the Waviness of the U-10Mo Coupon.....	3.4
Figure 3.4. (a) UTS as a Function of wt% Mo; (b) FEM Mesh.....	3.6
Figure 3.5. Flow Curve Used for U-10Mo Matrix Material during Hot Rolling.....	3.7
Figure 3.6. Experimental (a) and Simulated (b) Microstructures for U-10Mo Hot Rolled to 80% Reduction.....	3.7
Figure 3.7. Mo Concentrations (top) and Von Mises Stresses (bottom) in the FEM model after Compression Simulation for Three Material Conditions: As Cast, Homogenized at 800°C for 4 h, and Homogenized at 800°C for 48 h.....	3.8
Figure 3.8. Compressive Loads on Zr (red) and U-10Mo Interface in Three Conditions:	3.9
Figure 3.9. Zr Thickness Variation along Longitudinal Cross Sections	3.10
Figure 3.10. A Vector r with Length r and Angle θ in a Microstructure Domain	3.11
Figure 3.11. (a) Deformation Sequence of U-10Mo Microstructure; (b) Two-Point Correlation Functions along the Vertical Direction.....	3.12
Figure 3.12. (a) Approximation of the Particles Using Ellipses and (b) Variables Used in Stringer Identification Criteria in this Study.....	3.13
Figure 3.13. SEM Images of Initial Microstructures for Two Samples.....	3.14
Figure 3.14. SVF vs. Rolling Reduction for Two Samples	3.15
Figure 3.15. Maximum Stringer Length	3.16
Figure 3.16. Schematics for Near-Surface Particle Information.....	3.17
Figure 3.17. Evolution of Near-Surface Number of Particles and PVF during Rolling:	3.17
Figure 4.1. Strain from an FEM Simulation of Rolling to 65% Reduction	4.2
Figure 4.2. The Initial U-10Mo Microstructure, as Captured by EBSD.....	4.3
Figure 4.3. The U-10Mo Microstructure	4.3
Figure 4.4. The Recrystallization Progress of 78% Hot Rolled U-10Mo after annealing at 600°C and 700°C	4.4

Figure 4.5. The Grain Size Distribution of U-10Mo for One to Three Passes of 15% Rolling Reduction and 20 Minutes of Annealing at 700°C, Up to a Total of 45% Reduction in Thickness and 60 Minutes Annealing.....	4.5
Figure 4.6. (a) The Strain Distribution of U-10Mo for Hot-Rolling Reductions of 15%, 30%, and 45% with Intermediate Annealing Steps, Compared with the Strain Distribution of U-10Mo for a Single Hot-Rolling Pass to 45%.....	4.6
Figure 5.1. Roll-Separation Force as a Function of Number of Passes and Sample Exit Thickness using Different Roll Diameters.....	5.3
Figure 5.2. Roll-Separating Force as a Function of Thickness for Four Different Sample Widths at a 0.3 Friction Coefficient for the BWXT Cold-Rolling Mill.....	5.3
Figure 5.3. Flow Curve of U-10Mo Matrix Material at Room Temperature.....	5.4
Figure 5.4. The Finite-Element Cold-Rolling Model:	5.5
Figure 5.5. Simulated Particle Fracture (a) in Comparison with Experimental Microstructure (b).....	5.6
Figure 6.1. The Observed Recrystallization Progress of Cold-Rolled U-10Mo for 600°C and 700°C Anneals, Plotted Along with Their JMAK Equation Fits.....	6.1
Figure 6.2. Grain Structure Evolution and Recrystallization Kinetics from an Integrated Simulation of Successive Hot Roll and Cold Roll of U-10Mo, with Intermediate Annealing Steps.....	6.2
Figure 7.1. Average Grain Diameter of U-10Mo during Annealing at 700°C, 800°C, and 900°C	7.2
Figure 7.2. Stagnated Potts Model Microstructures Using Different Values of the Nonphysical Simulation Temperature T_s	7.3
Figure 7.3. The Average Grain Size of U-10Mo as Predicted by the Potts Model.....	7.4
Figure 8.1. Integration between Hot Rolling and Recrystallization.....	8.3

Tables

Table 4.1. Microstructural Information and its Significance in Fuel Processing/Performance	4.6
Table 5.1. Predicted and Measured Roll-Separation Force.....	5.1
Table 5.2. Predicted Achievable Thicknesses.....	5.2
Table 7.1. Potts Model Simulation Parameters.....	7.3

1.0 Introduction

First proposed in 2006, integrated computational materials engineering (ICME) has become an increasingly growing field in materials science and engineering (Allison et al. 2006a, b). The ICME concept has been acknowledged and implemented for modeling many different complex materials systems, as well as for the development of new materials (Allison et al. 2006, Backman et al. 2006, Cao et al. 2009, Joost 2012, Panchal et al. 2013, Li et al. 2015, Llorca et al. 2011). Material processing, which typically involves many complicated thermomechanical processes across very different time and spatial scales with a large number of material and processing parameters and design variations, is one important area that can take advantage of the ICME concept.

Conventional material process simulations often are used to model each individual process or phenomenon separately, without having the models communicate with each other. ICME augments information exchanges between relevant model components, which allows for prediction of the effects of the entire process on the microstructure. This paper represents a first attempt to apply ICME engineering to a uranium alloy with 10 weight percent molybdenum (U-10Mo), seeking better understanding of the microstructure resulting from thermomechanical processing.

Since the 1980s, the U.S. Department of Energy High Performance Research Reactor Conversion Program has investigated low-enriched uranium (LEU) as an alternative to highly enriched uranium. Because of its high density and favorable performance during fabrication and irradiation, U-10Mo has been identified as the most promising candidate LEU fuel (Burkes et al. 2010, Meyer et al. 2002, Snelgrove et al. 1997). U-10Mo alloy fabrication involves a complex series of material processing steps, including casting, homogenization, hot roll bonding of Zr interlayers, cold rolling, annealing, and hot isostatic pressing (HIP) (Sease et al. 2007, Wachs et al. 2008). Various analysis and modeling methods have been developed for many of these individual processes (Thomas 2002, Xu et al. 2016, Beynon and Sellars 1992, Pietrzyk and Lenard 2012, Ozaltun et al. 2013, Helle et al. 1985). However, the interaction and coupling between all individual model components has been lacking. Reliable predictions of the U-10Mo microstructure involving multiple process steps will not be possible without use of the ICME concept.

In previous U-10Mo modeling efforts (Ozaltun et al. 2011; Miller et al. 2010; Crapps et al. 2013; Hu et al. 2016; Soulami et al. 2014, 2015, 2016), material parameters were obtained from existing literature (Bostrom and Halteman 1956; Waldron et al. 1958; Craik et al. 1962; Butcher and Hatt 1964; Hills et al. 1964; Hoge 1966; DeMint et al. 2013; Devaraj et al. 2016a, b, c, 2017; Edwards et al. 2012; Gates et al. 1958; Henager et al. 2014; Jana et al. 2016; Joshi et al. 2016; Kautz et al. 2017a, b; McInnis et al. 2016; Nyberg et al. 2012, 2013, 2014, 2015; Prabhakaran et al. 2016a, b, 2017; Senor and Burkes 2014) or from extensive experiments carried out on U-10Mo samples. In addition, a complete understanding of the effect of processes, from casting through HIP, on the microstructure of U-10Mo is not feasible by conventional stand-alone models. An integrated process model of U-10Mo, based on the ICME concept, enables the information (model and materials parameters, etc.) to pass across different process models and provide a generic framework for modeling microstructure evolution of U-10Mo during a given series of thermomechanical processes.

A fully integrated model for all the processing components of U-10Mo is illustrated by Figure 1.1 and Figure 1.2. Figure 1.1 depicts a flowchart of key U-10Mo processes, the corresponding process models that will be integrated using ICME, and the output microstructure information of interest. The diagrams in the center row capture the main evolution features of microstructures, from initial as-cast status with

dendritic structures to final status after HIP with small and averaged grain distribution. All needed input parameters and expected output results from each process are marked in. Figure 1.2 shows all the developed computational tools and models and how they advance the modeling of the material processing.

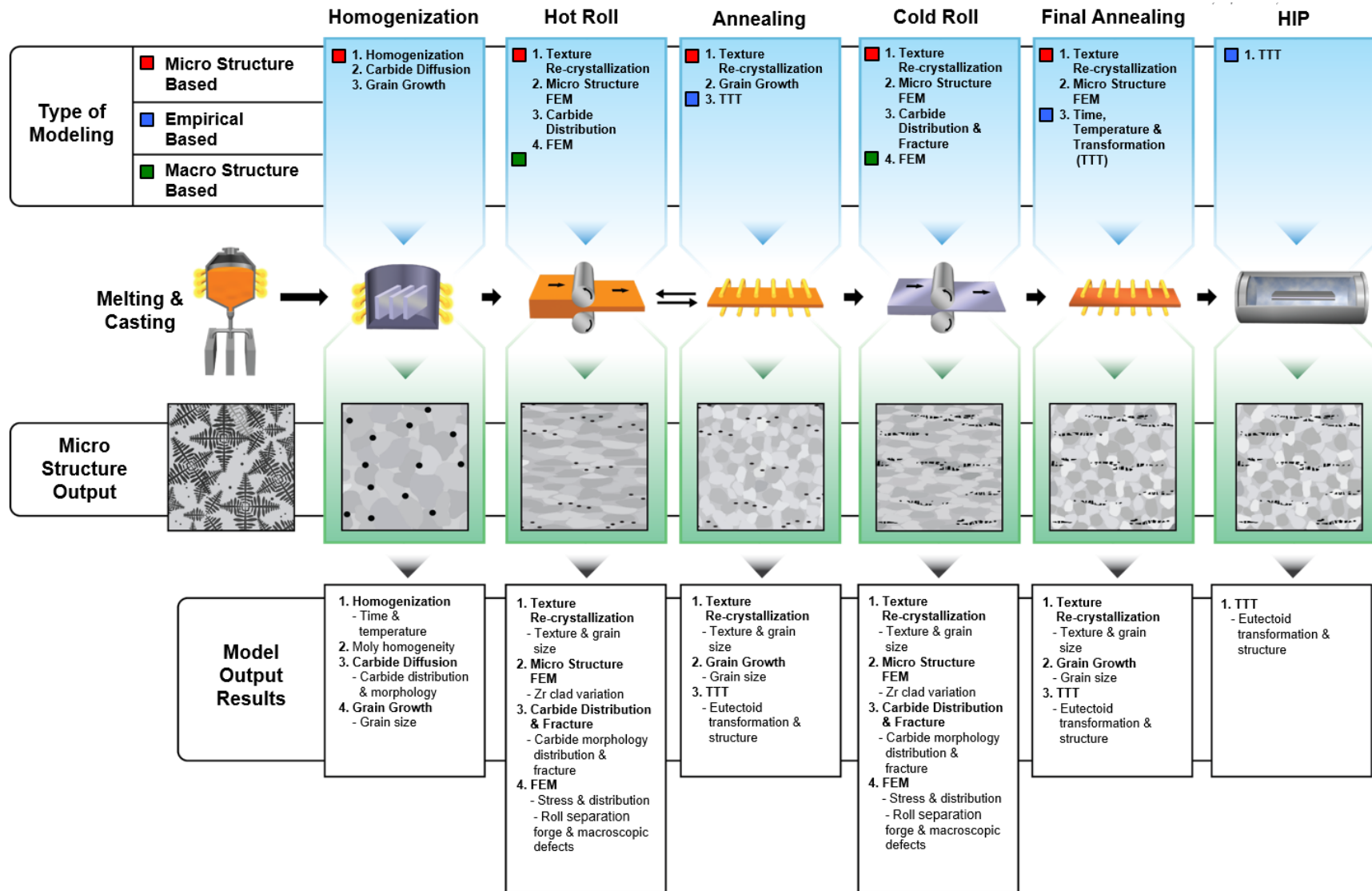


Figure 1.1. Inputs and Outputs of the Integrated Model for U-10Mo Processing

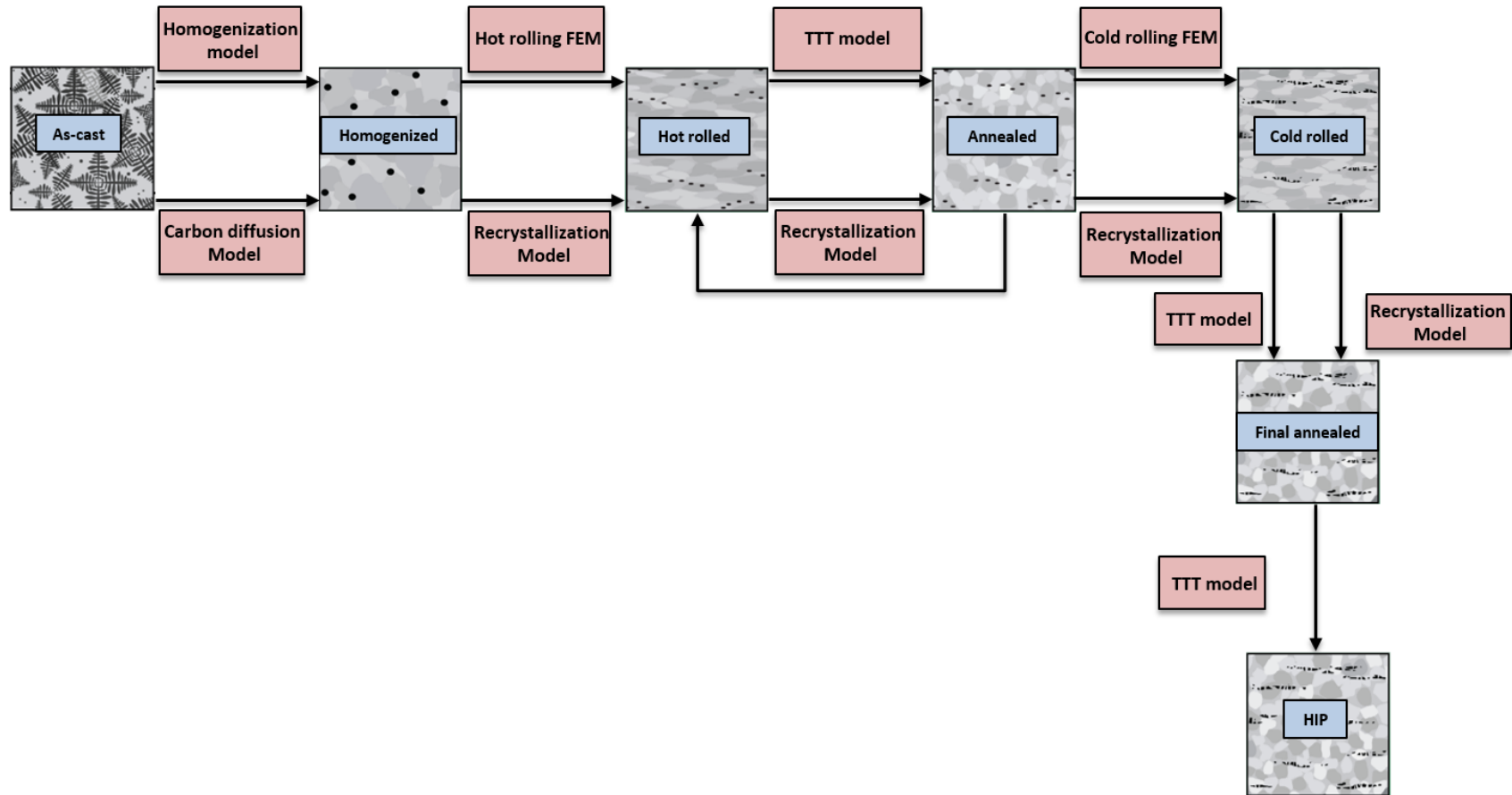


Figure 1.2. Integrated Model for Material Processing of U-10Mo

This report will focus on the integration processes from homogenization to cold rolling. It will describe the homogenization, carbon diffusion, hot and cold rolling FEM, and recrystallization models illustrated in Figure 1.2 but will not include Time Temperature Transformation (TTT) modeling. TTT modeling will be described elsewhere. Upon completion of casting, U-10Mo is heated to the γ -phase (above 560°C) for homogenization treatment to produce a more uniform molybdenum (Mo) distribution. During homogenization, molybdenum's dendritic structure is eliminated, and the Mo segregation is alleviated. All of these microstructural changes affect the behavior of U-10Mo in subsequent processes (Joshi et al. 2015a, b). Recently, Xu et al. (2016) proposed a homogenization model of U-10Mo as an alternative to time-consuming and labor-intensive experiments for optimizing the homogenization process. The homogenization model reconstructs the Mo concentration field from backscattered electron (BSE)-scanning electron microscopy (SEM) images of as-cast material. The proposed ICME for U-10Mo processes passes the microstructures reconstructed by the homogenization model from BSE-SEM images to a finite-element method (FEM) hot-rolling model of U-10Mo with Zr interlayers. The integrated model can predict the variation in the thickness of the Zr barrier as a function of the degree of homogenization. The information regarding the Mo concentration, carbide distribution, and grain morphology, i.e., the output of the homogenization model, is used as the input for the microstructure-based FEM hot-rolling model. To characterize carbide redistribution during the rolling, this model can be further integrated with the carbide distribution analysis to generate two-point correlation functions and obtain probability distributions of pair angles and particle size for the entire rolling process, and calculate the stringers or stringer-type particle volume fractions in different samples. The carbide distribution is a critical factor affecting the recrystallization, hardness, and fracture toughness of U-10Mo in subsequent processes (Meurling et al. 2001; Daigne et al. 1982). A macro-FEM hot-rolling model is a predictive tool used to optimize the hot-rolling schedule. It uses microstructure dependent mechanical properties of U-10Mo as inputs and predicts roll-separation forces and possible foil defects during hot rolling. The mechanisms of grain growth and recrystallization in the material during processing and fabrication of this fuel are not yet entirely understood. Processing variations often result in different grain morphologies, α -U precipitation at the grain boundaries from Mo solute depletion, and abnormal grain growth. To support consistent microstructure and performance of the alloy, and to identify processing pathways that avoid the detrimental effects of these phenomena, we integrated the FEM model with the Potts model to study U-Mo recrystallization and grain growth behavior as a function of rolling schedule, annealing temperature, annealing time, and starting microstructure. The FEM simulates the complicated deformation during rolling, while the Potts model uses the input of local deformation from FEM simulations to predict the recrystallization kinetics and the effect of material processes on microstructures. This is because the FEM simulates deformation well for a given microstructure, but not for a system with evolving microstructure. Meanwhile, the Potts model simulates recrystallization and grain growth, but cannot account for changes in shape. Therefore, integrating the FEM model with the Potts model enables simulation of microstructural evolution during complicated materials processes during which large deformations and recrystallization occur. Along with carbide redistribution during hot rolling, hard particle fracture is also observed during the cold-rolling process (Joshi et al. 2015b). The fractured particles can be the sources of crack initiation in the U-10Mo matrix and cause eventual mechanical failure of such materials; thus, understanding the distribution and mechanism of fracture of these carbides is desirable. A macro-FEM cold-rolling model was developed to investigate the effect of roll diameter, tensioning, and reductions on the ability to attain the desired foil thickness without overstressing the material.

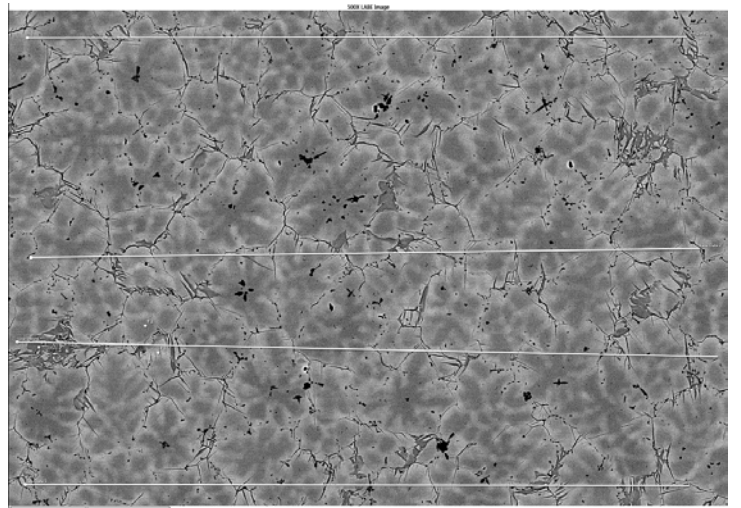
In this report, emphasis is placed on interfacing these model components, which enables accounting for the microstructural variations that occur during these processes. The resulting integrated model should provide a better understanding of the evolution of U-10Mo during fabrication and also provide quantified measurement of the effects of different process parameters on the microstructure and mechanical behavior

of U-10Mo. Based on the results from the integrated model, the U-10Mo fabrication process can be optimized in order to obtain high quality U-10Mo samples at reduced time and cost.

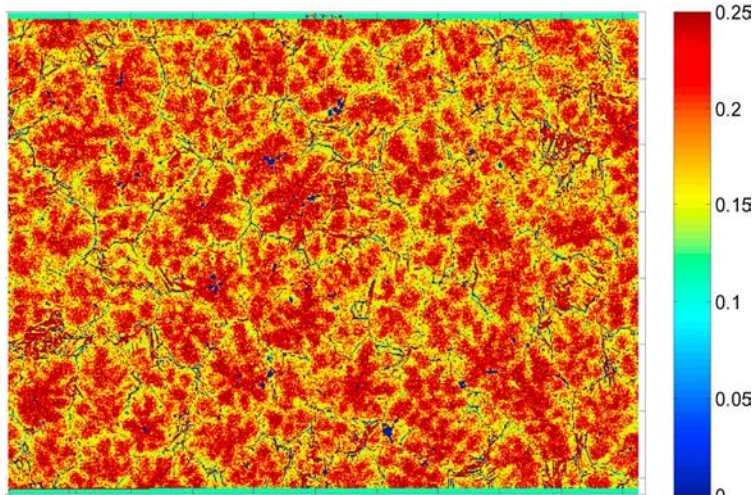
2.0 Homogenization

2.1 Model Description

In this section, a brief description of the statistical model used to reconstruct Mo concentration from any given BSE-SEM image with energy dispersive spectroscopy (EDS) line scans is introduced. The Mo concentration over the entire domain can be constructed pixel by pixel based on a nonlinear relationship between BSE-SEM image gray scale and EDS line data. Details about this technique can be found in Xu et al. (2016). The relationship between gray scale and Mo concentration is constructed by plotting the concentration as a function of the gray scale value. Figure 2.1(a) shows a BSE-SEM image of an as-cast U-10Mo sample, and Figure 2.1(b) presents a reconstructed Mo concentration map of the sample with Mo-rich and Mo-lean regions clearly identifiable by color. The carbide particles are represented by blue regions with zero Mo concentration. The morphology of carbide particles is also well preserved in the reconstructed concentration maps.



(a)



(b)

Figure 2.1. Images of As-Cast U-10Mo: (a) BSE-SEM Micrograph with Line Scans; (b) Mo Atomic Concentration Reconstruction

2.2 Model Validation

The homogenization kinetics is dominated by diffusion-induced dissolution of segregated Mo. The proposed model considers the diffusion of Mo in U-10Mo:

$$\frac{\partial c}{\partial t} = \nabla(D\nabla c), \quad (2.1)$$

where $c(x,t)$ is the atomic concentration of Mo at given location x and time t . Mo intrinsic diffusivity is dependent on the Mo concentration, and D is the effective diffusion constant of Mo at the temperature of homogenization. The proposed partial differential equation can be solved using the finite difference method by discretizing the domain and approximating the first-order derivative for time and the second-order derivative for space.

With the reconstructed Mo concentration map in Figure 2.1(b) and the simulation method described in the previous paragraph, we can implement the homogenization simulations to obtain the homogenization kinetics. The quantitative measure for homogenization, $\Delta c = c_{95\%} - c_{5\%}$ (where $c_{critical_p}$ is the concentration at which the probability $P(c < c_{critical_p}) = critical_p$, and $critical_p$ can be 95% or 5%), can be obtained both from simulations and from experimental BSE-SEM images at different homogenization times and temperatures. The direct comparison between simulations and experiments is presented in Figure 2.2, where square symbols represent the quantitative measurements from experiments at 800°C for pin casting samples, and the line shows results of the homogenization simulations that used the reconstructed concentration map of the as-cast sample as the input. Both experiment and simulation show a trend of homogenization with decreasing quantitative measure Δc . The diffusion coefficient used for Mo diffusion was chosen as $D = 10^{-16} \text{ m}^2/\text{s}$ to fit the simulated homogenization kinetics. The Mo intrinsic diffusivity in U-10Mo is nonuniform and highly dependent on the local Mo concentration.

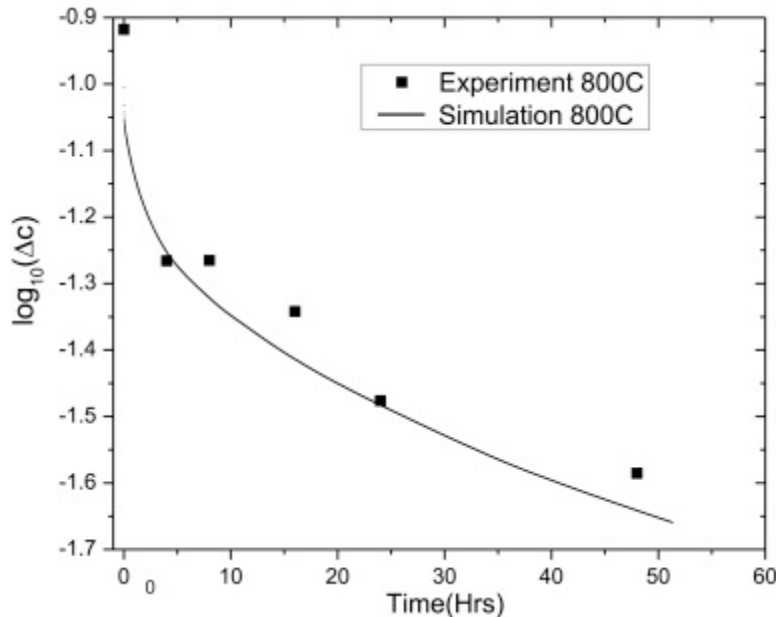


Figure 2.2. Homogenization Kinetics from Simulation (line) and Experimental BSE-SEM Images (squares for 800°C)

2.3 Impact for the Program

The modeling work developed here has been applied to provide guidance on the homogenization time required for LANL Y-12 LEU-Mo sample. The homogenization time is critical to the evolution of final microstructure and need to be determined before the actual homogenization process. Here we first obtained the backscattered electron (BSE) images of Y-12 LEU-Mo samples and the corresponding line-scan data of Mo concentration. Using the methodology introduced in the previous section, we reconstructed the Mo concentration for top, middle, and bottom sections, as shown in Figure 2.3.

Homogenization kinetics can be obtained by running the homogenization simulation for the bottom section of the sample. The homogenization time of a Y-12 LEU-Mo sample can be estimated by comparing with the A3-90 sample, a smaller grain size sample than the Y-12 material. The simulated kinetics for both samples are presented in Figure 2.4, which indicates the Y-12 LEU-Mo sample has a much slower homogenization kinetics than the A3-90 sample. The BSE images for two samples are different. The Y-12 LEU-Mo sample has a resolution of 2.5 $\mu\text{m}/\text{pixel}$ and that for A3-90 has a much higher resolution of 0.55 $\mu\text{m}/\text{pixel}$. The diffusion length l_0 can be estimated from the kinetics, with $l_0 = 2.8 \mu\text{m}$ for the Y-12 LEU-Mo sample and $l_0 = 1.6 \mu\text{m}$ for the A3-90 sample. This intrinsic diffusion length is different from the grain size or the distance between second-order dendrite branches, but it seems proportional to them. It can be quantitatively determined from the homogenization simulations for complicated microstructure.

Since the homogenization time required for the same level of Mo homogeneity is proportional to the square of the diffusion length, Y-12 LEU-Mo requires about $(2.8/1.6)^2 = 3.06$ times the homogenization time of A3-90 in order to achieve the same level of homogeneity. This means homogenization for at least 144 h is needed for Y-12 LEU-Mo to achieve the same homogeneity of A3-90 at 48 h.

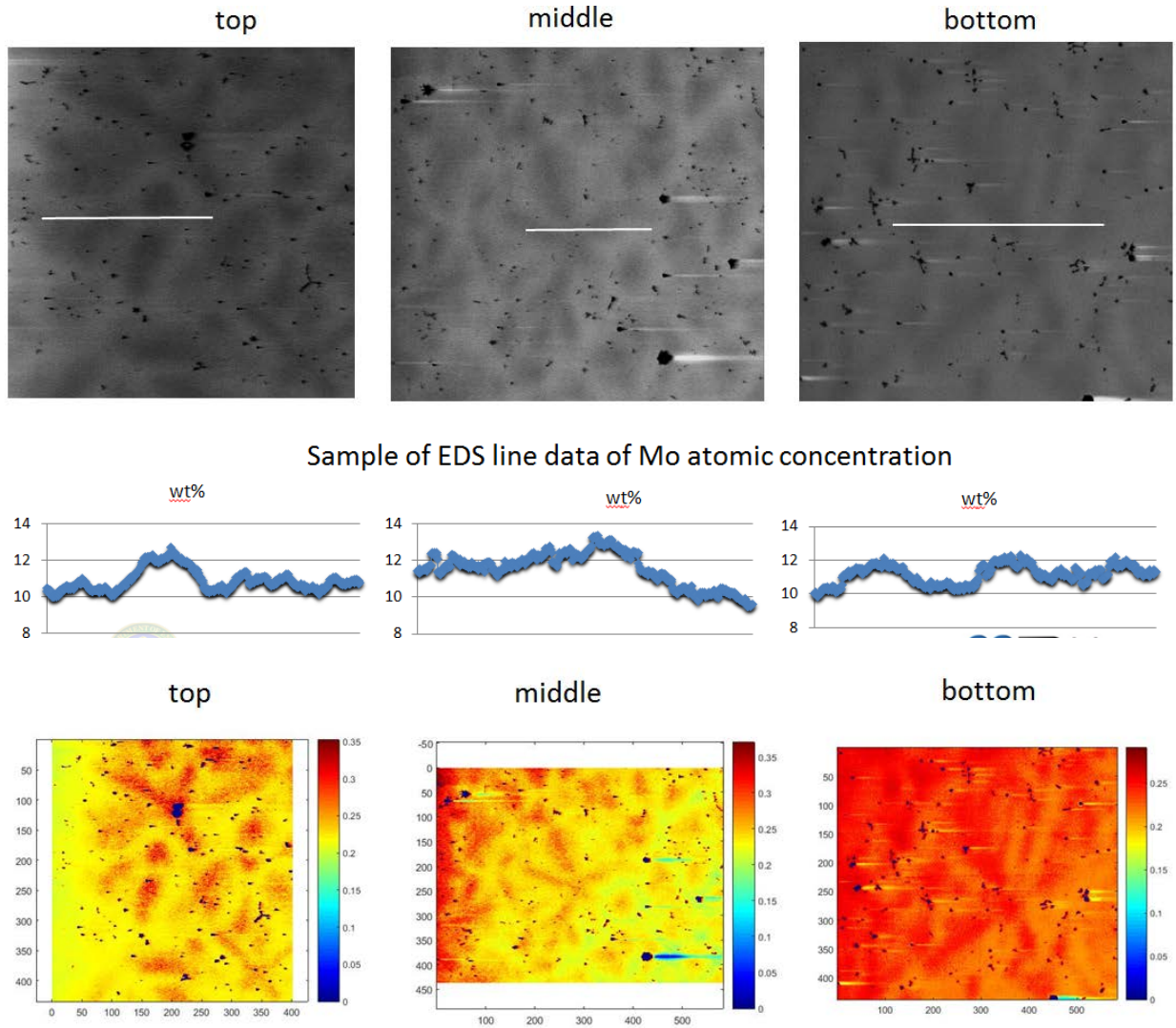


Figure 2.3. BSE-SEM Images, Mo Atomic Concentration along the EDS Lines, and the Reconstructed Mo Concentrations for Top, Middle and Bottom Sections of Y-12 LEU-Mo Sample

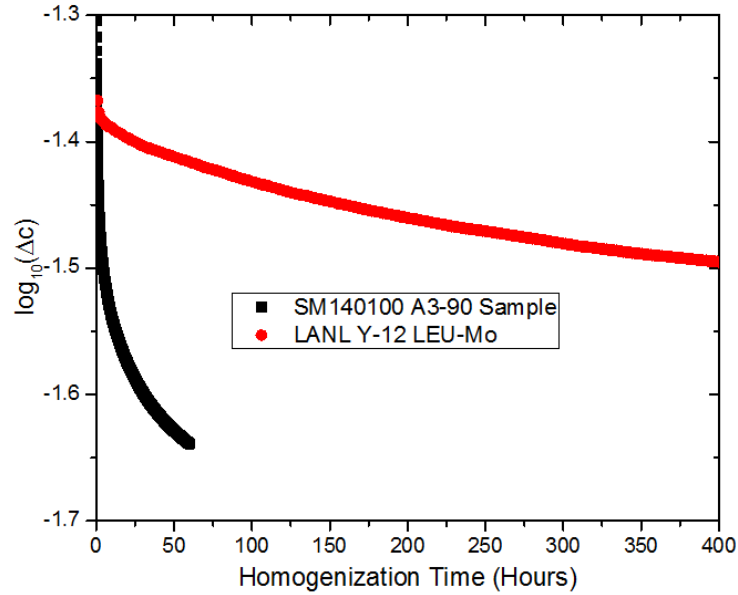


Figure 2.4. Simulated Homogenization Kinetics for A3-90 and Y-12 LEU-Mo Samples

2.4 Tools Developed

2.4.1 Determine Sample Qualification

Homogenization heat treatment is performed to attain uniformity in microstructure, which helps to achieve the desired workability and microstructure in final products, and eventually to gain predictable and consistent performance. In this section, we propose a simple metric/criterion to determine sample qualification after homogenization treatment using statistical methods (Wang et al. 2019). The given qualification specification for U-Mo fuel plate described in SPC-1691 (INL 2017) is quoted herein: “A sufficient number of samples shall be randomly taken from a sufficient number of fuel plates randomly selected from a fuel plate lot to allow statistical determination of 95% confidence that 95% of the U-Mo has 10.0 ± 1.0 weight percent (wt%) Mo microscopically throughout the U-Mo.” The requirements can be interpreted as a general two-sided tolerance interval (TI) problem. More specifically, a general two-sided TI on a normal distribution has confidence $\gamma \times 100\%$ of containing at least $p \times 100\%$ of the distribution. The limits of the two-sided TI, Y_L and Y_U , are defined as

$$Y_L = \bar{Y} - k_2 s, \quad (2.2)$$

$$Y_U = \bar{Y} + k_2 s, \quad (2.3)$$

where \bar{Y} and s are the sample mean (10 wt% Mo) and sample standard deviation of a given sample size N , respectively. Note that the sample size, N , indicates the number of measurements of Mo composition (wt%) when performing EDS line-scan experiments. In this case, Y_L and Y_U based on the problem statement above are 9 wt% and 11 wt%, respectively. With a constant $\bar{Y} = 10\%$ assumed for all samples, the original qualification statement can be equivalently interpreted as follows: find the appropriate sample size N that leads to the given TI bounded between Y_L and Y_U . The sample standard deviation s can be calculated as

$$s = \sqrt{\frac{\sum_{i=1}^N (Y_i - \bar{Y})^2}{\nu}}, \quad 2.4$$

where Y_i is the Mo wt% obtained from each measurement, and $\nu = N - 1$ represents the degrees of freedom. The computation of the two-sided k_2 factor can be approximated as

$$k_2 \approx \left(\frac{\nu \left(1 + \frac{1}{N}\right) z_{\frac{1-p}{2}}^2}{\chi_{1-\gamma, \nu}^2} \right)^{\frac{1}{2}} \quad 2.5$$

where $\chi_{1-\gamma, \nu}^2$ is the critical value of the chi-squared distribution with degree of freedom ν . The chi-squared value indicates that it is $\gamma \times 100\%$ possible to observe a value that is greater than $\chi_{1-\gamma, \nu}^2$. Additionally, $z_{(1-p)/2}$ is the critical value of the standard normal distribution associated with cumulative probability of $(1 - p)/2$. Based on the specification statement from SPC-1691, we can set $p = \gamma = 0.95$. The value of $\chi_{1-\gamma, \nu}^2 = \chi_{0.05, N-1}^2$ can be determined for any given N . And the value of z can be calculated as $z_{(1-p)/2} = z_{0.025} = -1.96$. Now, k_2 is only a function of sample size, N . After k_2 is calculated, the qualification for any given plate can be determined using Equations 2.2 and 2.3.

Next, we provide a general recommendation for the optimal number of measurements to determine fuel plate qualification if no available measurement data exist in advance. A plot of k_2 versus N , shown in Figure 2.5, shows that k_2 gradually decreases (black line) but its slope slowly increases (red line) with increasing N . The value of k_2 eventually approaches an asymptote of ~ 2 . A gradient of $k_2 > -0.1\%$ can be considered a mathematical indication of stability. The corresponding value of N at $\frac{dk_2}{dN} = -0.1\%$ is 133, and the associated measurement time (~ 2 h) is experimentally affordable. Therefore, it is reasonable to select $N = 133$ as the suggested number of measurements to determine the fuel plate qualification, resulting in $k_2 = 2.19$. During data collection, measurements should be discarded if Mo weight percentage is outside the range of 7–13% to avoid the influence of carbides. Also, the collected data must be spatially independent.

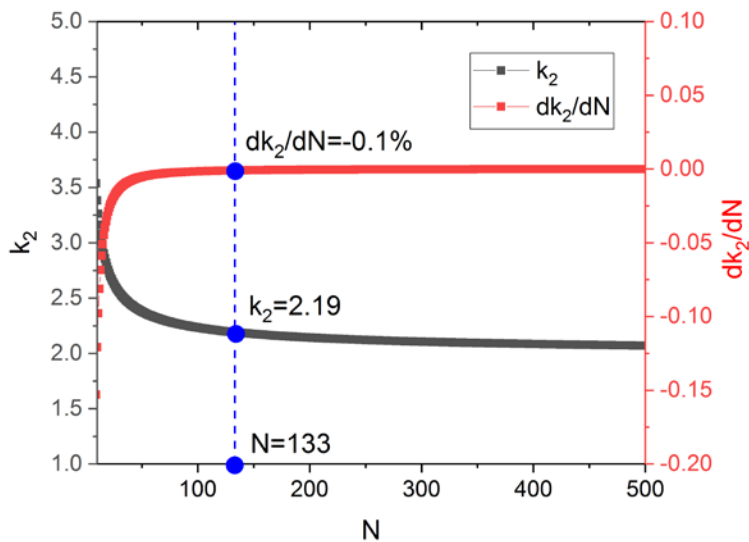


Figure 2.5. Relationship of k_2 and its Gradient to N

2.4.2 Determine Homogenization Time and Temperature

Another tool that we developed is a MATLAB based toolbox that can be used to determine the homogenization time and temperature. More specifically, for any given reconstructed U-10Mo microstructure, this tool can help estimate the required time to reach desired homogenization level at any homogenization temperature by solving the diffusion-induced dissolution of segregated molybdenum as shown in Equation (2.6):

$$\frac{\partial c}{\partial t} = \nabla(D\nabla c), \quad 2.6$$

Where $c(x,t)$ is the atomic concentration of Mo at a given location x and time t . Mo intrinsic diffusivity is dependent on the Mo concentration, and D is the effective diffusion constant of Mo at the temperature of homogenization. The quantitative measure $\Delta c = c_{95\%} - c_{5\%}$ (where $c_{critical_p}$ is the concentration at which the probability $P(c < c_{critical_p}) = critical_p$, and $critical_p$ can be 95% or 5%) is used to determine the level of homogenization attained for any given homogenization period.

3.0 Hot Rolling

3.1 Macro-FEM Model

3.1.1 Model Description

The commercial FEM code LS-DYNA® was used to develop a macroscopic model to simulate hot multipass rolling. Coupled thermal-structural analysis, using elastic-plastic-thermal constitutive equations, was adopted to describe the material behavior. The rolling setup consisted of two rolls and a roll pack made up of a coupon and the can material. The model also takes into account the temperature decrease due to contact between the roll pack and the rolls. An initial temperature, which is considered uniform on all the nodes, is applied to the roll pack at the beginning of every pass. This temperature is calculated taking into account the temperature loss due to radiation to the surrounding air during the transfer from the exit of the rolls back to the entrance of the rolls, or from the furnace to the entrance of the rolls when reheats are necessary. While the rolls are considered to be rigid material, the can (AISI 1018 steel) and the alloy coupon (U-10Mo) were modeled using the *MAT_ELASTIC_PLASTIC_THERMAL material card in LS-DYNA. This constitutive model is temperature dependent and suited to modeling isotropic plasticity at high temperatures. This elastic-plastic model is computationally efficient and needs only a few parameters.

The model was first validated through comparison with actual rolling data, and then used to perform various parametric studies investigating the effect of can material on the rolled sheet defects and the effects of roll diameters and coupon geometries on the roll-separating forces. This modeling tool can be used by fuel manufacturers to design their rolling schedules and select the appropriate equipment. Foundation of this work and a parametric study using the FEM model can be found in (Soulami et al. 2014, 2015, 2017)

3.1.2 Model Validation

This approach used to develop the model was validated through comparison with data from literature as well as experimental data performed at Pacific Northwest National Laboratory (PNNL) (Joshi et al. 2015b). Figure 3.1 represents a comparison between measured roll-separating force and model predictions using properties from the literature (Simulated Separation Force 1) and from PNNL compression tests (Simulated Separation Force 2). The material work-hardening for temperatures below 550°C was taken into account in the simulated roll-separating force, which is in a better agreement with the measurements. We can clearly observe the shift to the top of the roll-separating force curve after introducing the work-hardening observed in compression tests. Note that the forces predicted using PNNL compression data deviate less than 3% over the entire rolling schedule, whereas the forces predicted using literature data deviate ~7% from the measurements.

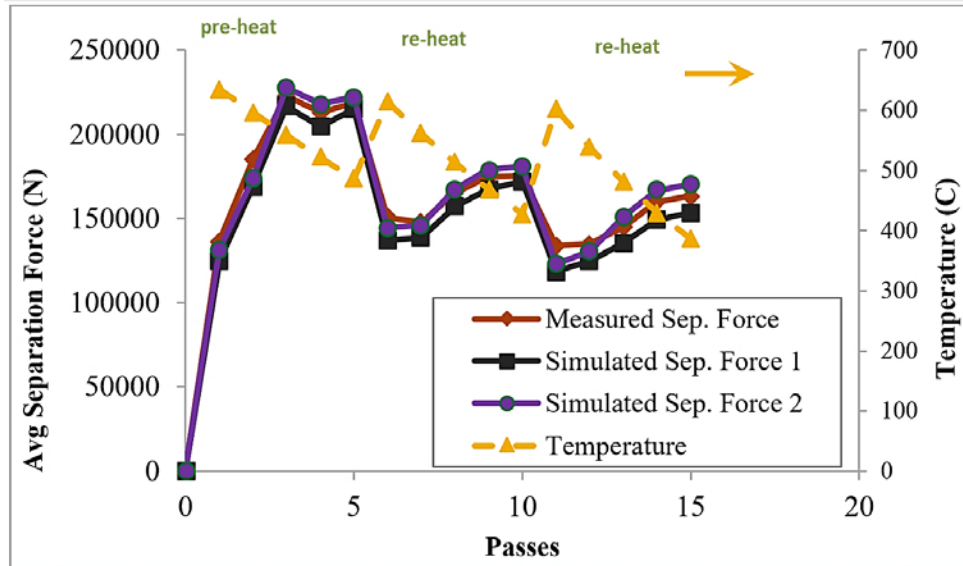


Figure 3.1. Measured Separation Forces Compared to Simulated Separation Forces (using mechanical properties from (1) the Literature and (2) PNNL Compression tests) for 15 Passes

3.1.3 Impact for Program

This hot-rolling model was crucial in helping BWX Technologies (BWXT) optimize their rolling schedule and switch from low reduction passes to high reduction passes. The model was able to provide them with the predicted roll-separation forces, torque, and through-thickness strains. The model suggested that 40% reduction could be achieved on the BWXT 16" diameter rolling mill without exceeding the mill load capacity. Along with microstructural findings on recrystallization, through-thickness strain was also predicted by the model and used to select the appropriate reduction and help minimize rolling defects.

The model was also used to predict rolling defects due to can material. Four cases were considered in this parametric study: (1) rolling of a U-10Mo coupon inside a 1018 steel can, (2) rolling of a U-10Mo coupon inside a 304 stainless steel can, (3) rolling of a U-10Mo coupon inside a Zircaloy-2 can, and (4) bare rolling of a U-10Mo coupon. To quantify in the simulations the dog-boning that had been observed in practice, the thickness variation along the centerline of the U-10Mo sheet was plotted, as shown in

Figure 3.2. Thickness was measured at 50 equidistant points from one end of the coupon to the other, lengthwise along the midplane of the alloy coupon. For the 1018 steel can, dog-boned areas showed a ~25% thickness increase with respect to the average thickness in the remaining part of the coupon. In the case of rolling inside the 304 stainless steel can, about a 19% increase in thickness was observed, whereas in the case of rolling inside a Zircaloy-2 can, only ~15% increase in thickness at the edges of the U-10Mo coupon was observed. The bare-rolling case does exhibit no dog-boning, and relatively uniform thickness along the coupon. Dog-boning amplitude is inversely proportional to the strength of the can material. In fact, the stronger the can material, the less likely localized thickening of the fuel alloy and thinning of the cladding at the edges of the fuel meat will be observed.

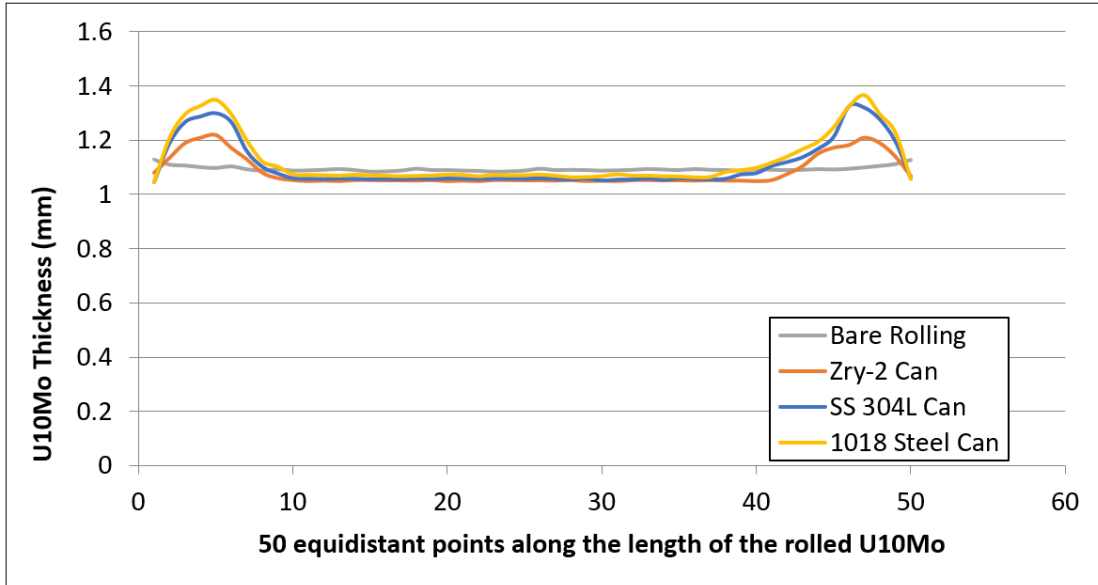


Figure 3.2. Thickness Variation Across the Length of the U-10Mo Coupon in the Cases of (1) Rolling Inside a 1018 Steel Can, (2) Rolling Inside a 304 Stainless Steel Can, (3) Rolling Inside a Zircaloy-2 can, and (4) Bare Rolling

Waviness of the rolled sheet pack is also observed in hot rolling canned fuel. This waviness was measured and is represented in Figure 3.3, comparing coupons rolled inside a 1018 steel can, rolled inside a Zircaloy-2 can, and rolled bare. The picture in the plot represents a longitudinal cross section of the U-10Mo coupon along the midline. Point #1 is located at the left bottom corner of the cross section. Vertical distances between Point #1 and Points #2–13, all located at the bottom surface of the alloy coupon, have been measured, and values are reported on the plot. Waviness is more pronounced in the case of rolling in a 1018 can than in a 304 stainless steel can or a Zircaloy-2 can, and almost no waviness is present in the bare-rolling case. In general, this defect can result from various aspects of the rolling process, including bending of the rolls, variation of the roll-separation force along the sheet, or dog-boning. As stated before, because no deformation of the rolls is present in our modeling approach, we only focus on waviness causes other than bending and flattening of the rolls. The gap between surfaces of the fuel core and the can’s picture frame appears to be the major contributor to this defect. This gap results from the mismatch of strength between the U-10Mo coupon and the can material. A sudden change in the material resistance, when the rolls reach the fuel core, leads to an increase in the roll-separation force, and therefore to the initiation of the waviness of the sheet. Figure 3.2 also shows the

relatively uniform bare-rolled U-10Mo coupon, where no dog-boning, waviness, or thickness variation in any direction are observed in the predicted bare-rolled sheet.

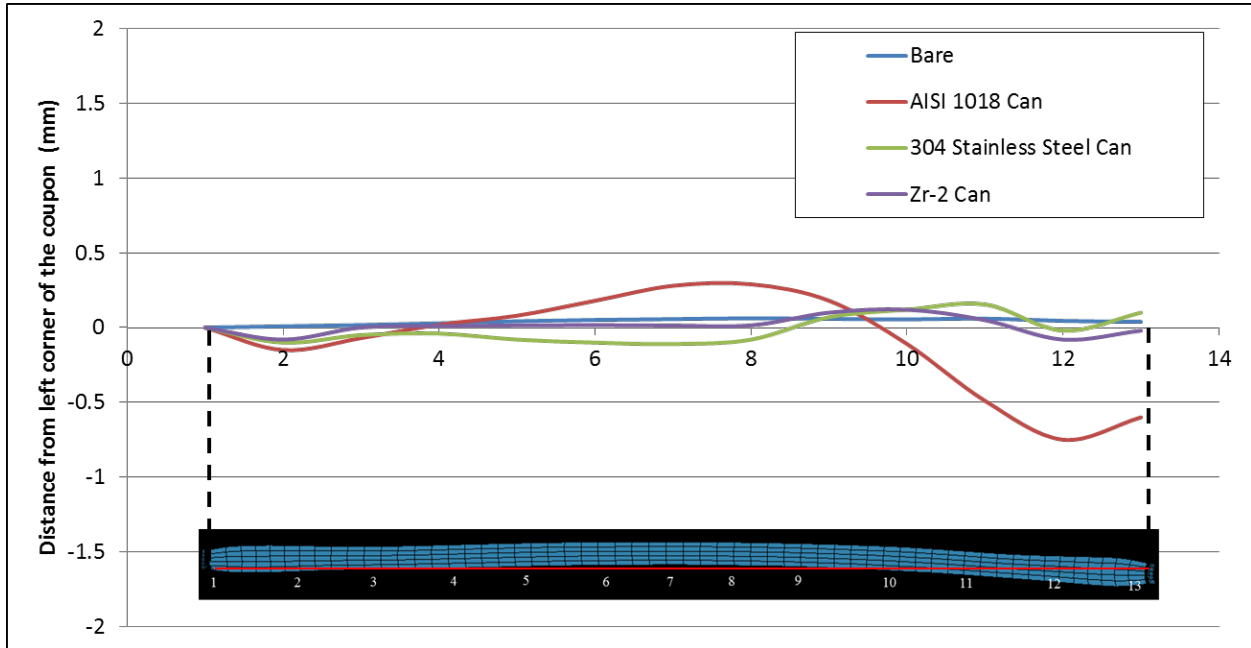


Figure 3.3. Representation of the Waviness of the U-10Mo Coupon

3.1.4 Tools Developed

A multipass hot-rolling finite-element analysis (FEA) model was developed in LS-DYNA. The model has the capability to investigate the effect of roll diameter, U-10Mo sample geometry, can material and geometry, rolling speed, and temperature.

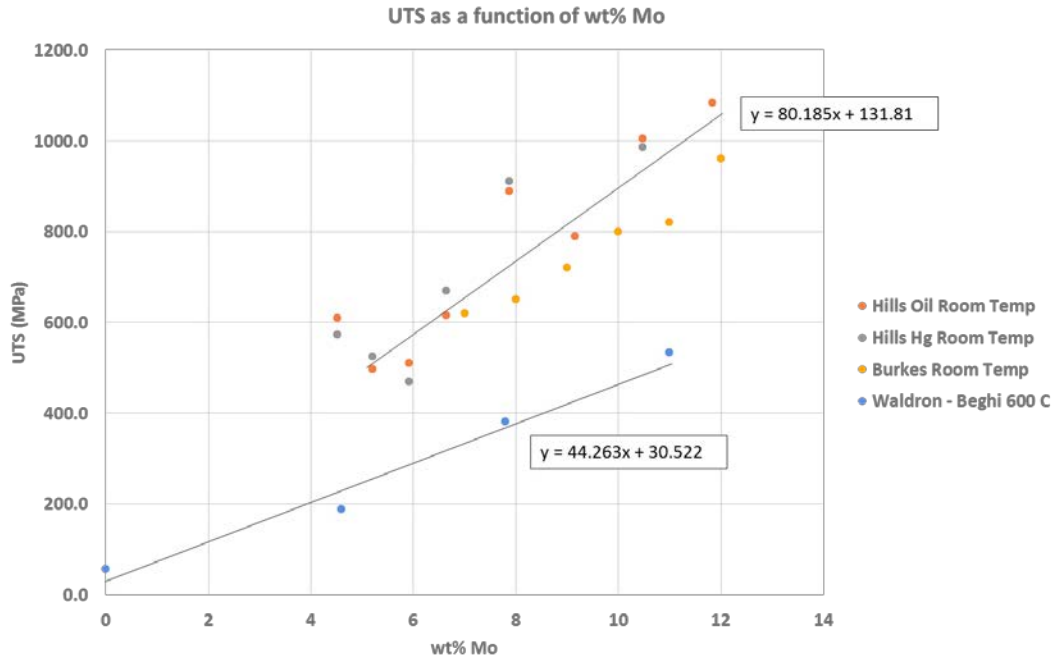
3.2 Microstructure-Based FEM Model

As the second component of the integrated model, the microstructures generated from the homogenization model were used to build a microstructure-based FEM model for compression and rolling simulations. Because one of the defects observed in U-10Mo fuels is nonuniform Zr coating thickness (Edwards et al. 2012), the model investigates the effect of homogenization on the variation of U-10Mo/Zr thickness in as-rolled fuel foils. To better understand the potential variables associated with Zr thickness, a microstructure-based FEM model was developed to study the effect of homogenization on the U-10Mo/Zr interaction during rolling. This model uses reconstructed microstructures from the homogenization model as input.

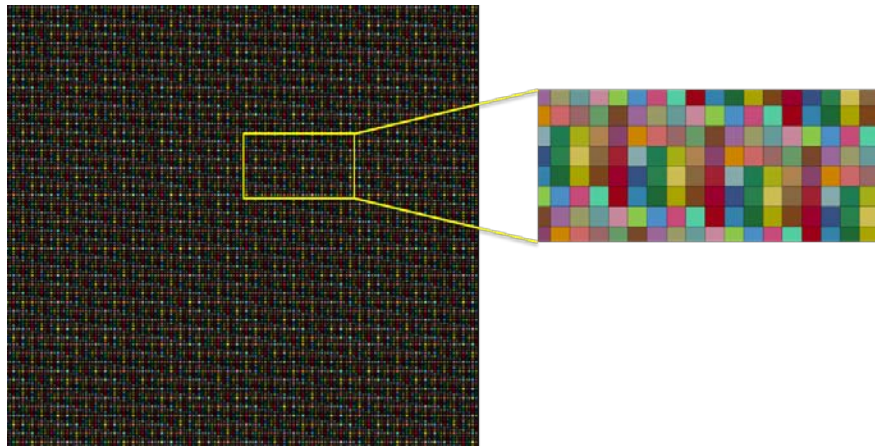
In addition, the influence of initial carbide particle distribution features on the evolution of particle distribution and stringer distribution within the U-10Mo alloy during hot rolling was investigated using synthetic microstructure-based FEM models. Stringer statistics analyses and two-point correlation functions (2PCFs) were then performed on the simulated results. Stringer volume fractions (SVFs), maximum stringer lengths, and 2PCF curves were compared among the models with different initial microstructural features. Evolution of near-surface particle distributions during rolling were also examined.

3.2.1 Model Description

To build the microstructure-based FEM model for Zr thickness analysis, the Mo concentration was correlated with mechanical properties. Figure 3.4(a) plots ultimate tensile strength (UTS) as a function of Mo concentration (Waldron et al. 1958; Hills et al. 1964; Beghi 1968; Burkes et al. 2009a). Linear regression fit lines were used to establish the relationship between Mo concentration and UTS of the U-10Mo alloy, as shown in Figure 3.4(a). A two-dimensional FEM model was created, with each element assigned mechanical properties based on its Mo concentration using the built correlation functions. A MATLAB script was programmed to generate the FEM input file. The commercial FEM code LS-DYNA was used to conduct the simulations using an explicit formulation. Elements with Mo concentration below 0.1% are considered carbides, which are purely elastic. Figure 3.4(b) plots representative volume elements (RVEs), with each color representing one element with a given Mo concentration and the corresponding mechanical properties.



(a)



(b)

Figure 3.4. (a) UTS as a Function of wt% Mo; (b) FEM Mesh

For carbide particle distribution analysis, simple plane-strain compression simulation was applied. All the microstructures generated after homogenization were converted to plane-strain FEM models. The commercial FEM code ABAQUS/Explicit was used for the simulations in this study. A multipoint constraint was applied to keep the right and left edges of the model straight vertically during the compression (i.e., rolling) process. The flow behavior of the matrix material was assumed to be isotropic with an elastic modulus of 65 GPa; the flow curve adopted in the simulation is presented in Figure 3.5 (Wang et al. 2017).

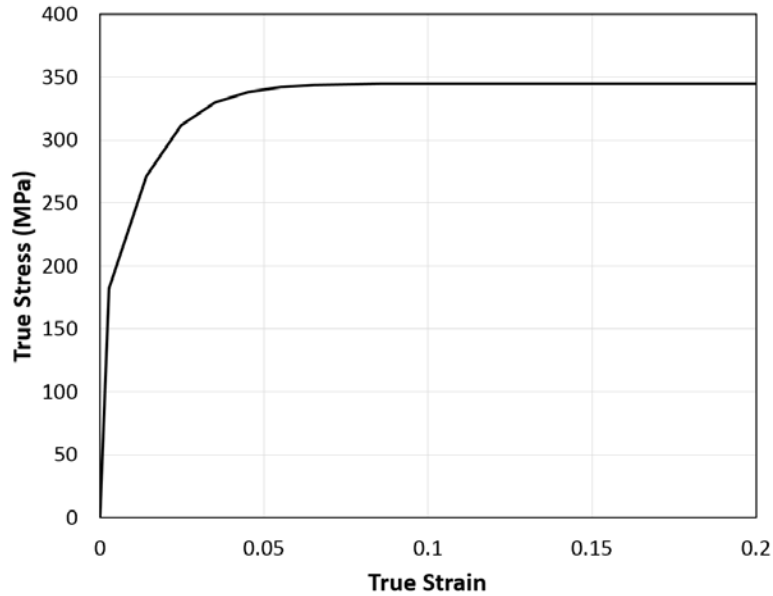


Figure 3.5. Flow Curve Used for U-10Mo Matrix Material during Hot Rolling

3.2.2 Model Validation

We did not perform validation tests to predict Zr thickness. However, a validation study was performed by comparing the FEM simulation results with an experimental image for a hot-rolling process from 0 to 80% reduction. The experimental microstructure data for particle distributions at the intermediate hot-rolling reductions of 40% and 65% are not available for comparison with simulation results, so only a comparison for 80% reduction can be made (Figure 3.6a). Comparing the simulated (Figure 3.6b) and experimental microstructures (Figure 3.6a) shows that the two have rather similar features of particle distribution (Hu et al. 2018).



(a) Experimental



(b) Simulations

Figure 3.6. Experimental (a) and Simulated (b) Microstructures for U-10Mo Hot Rolled to 80% Reduction

3.2.3 Impact for Program

To investigate the effect of homogenization on the U-10Mo/Zr interface using the microstructure-based FEM model, three cases were selected: as-cast material, material homogenized for 4 h at 800°C, and material homogenized for 48 h at 800°C. FEM models were created for each of the three conditions, and slight compression corresponding to 4% thickness reduction was applied to these RVEs. Results show that the Mo segregation is captured by the models in terms of differences in local stresses.

In Figure 3.7, images 1-a, 1-b, and 1-c represent the Mo concentrations in as-cast and homogenized conditions. Images 2-a, 2-b, and 2-c represent the local von Mises stresses in the microstructures after compressive loading. Homogenization eliminates the dendritic structure, mainly present in the as-cast condition, where differences in Mo concentrations causes high stresses in the cores of the grains (Mo-rich regions) and low stresses at the grain boundaries (Mo-lean regions). The inclusions (carbides), which correspond to Mo-lean areas (blue) with concentrations less than 2%, are present in the FEM model and have lower stresses. Grains are clearly marked in the homogenized microstructures and are also evident in the FEM model (images 2-b and 2-c).

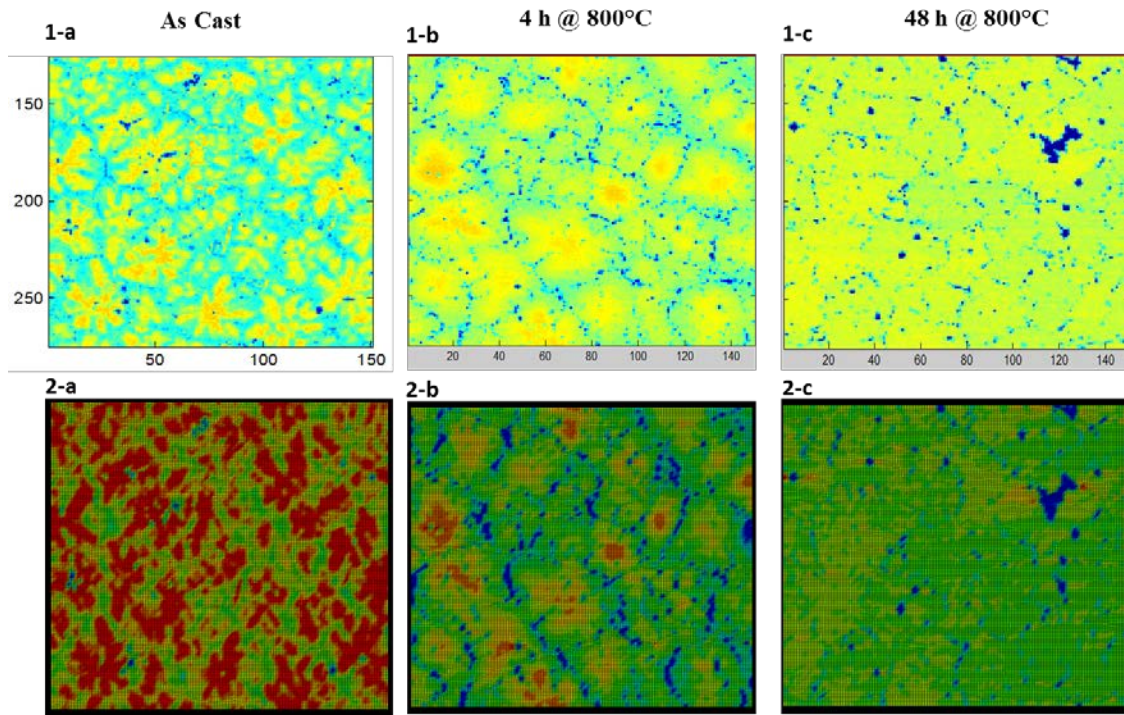


Figure 3.7. Mo Concentrations (top) and Von Mises Stresses (bottom) in the FEM model after Compression Simulation for Three Material Conditions: As Cast, Homogenized at 800°C for 4 h, and Homogenized at 800°C for 48 h

Next, a 25 μm thick Zr layer is added on top of the U-10Mo RVE. Compressive loads corresponding to 7% thickness reduction are applied to the top of the Zr layer to simulate rolling conditions and investigate the effect of deformation on the Zr clad variation at 600°C. Isotropically uniform mechanical properties for Zircaloy-4, extracted from Garde (1977), are assigned for the Zr. U-10Mo mechanical properties at 600°C are presented in Figure 3.4. A closer look at the Zr thickness reveals that the model predicted a nonuniform thickness in the case of as-cast U-10Mo. Waviness is observed in Figure 3.8(a), which is due to the differences in Mo concentration and, therefore, is apparent in stresses in the RVE. Thinning of the Zr layer is less pronounced for the two levels of homogenization studied in this work, 800°C for 4 h and 48 h, represented in Figure 3.8(b) and Figure 3.8(c), respectively. Homogenization reduces the variability of the Zr layer thickness. In Figure 3.9, the nonuniformity of the Zr clad thickness is quantified by plotting the Zr layer thickness along the longitudinal cross section of the rolled RVE. For the as-cast model, the Zr layer varies as much as 4 μm , and in the 800°C for 48 h model, it varies less than 1 μm . During this deformation, the carbides are shown to have very little to no effect on Zr clad variation. These results suggest that a large gradient in material strength within the U-10Mo alloy is undesirable and may be detrimental to the Zr/U-10Mo interface uniformity. In fact, given the fact that a uniform stress

distribution in the U-Mo is the best way to avoid Zr thinning, homogenization would improve the Zr interlayer thickness variation.

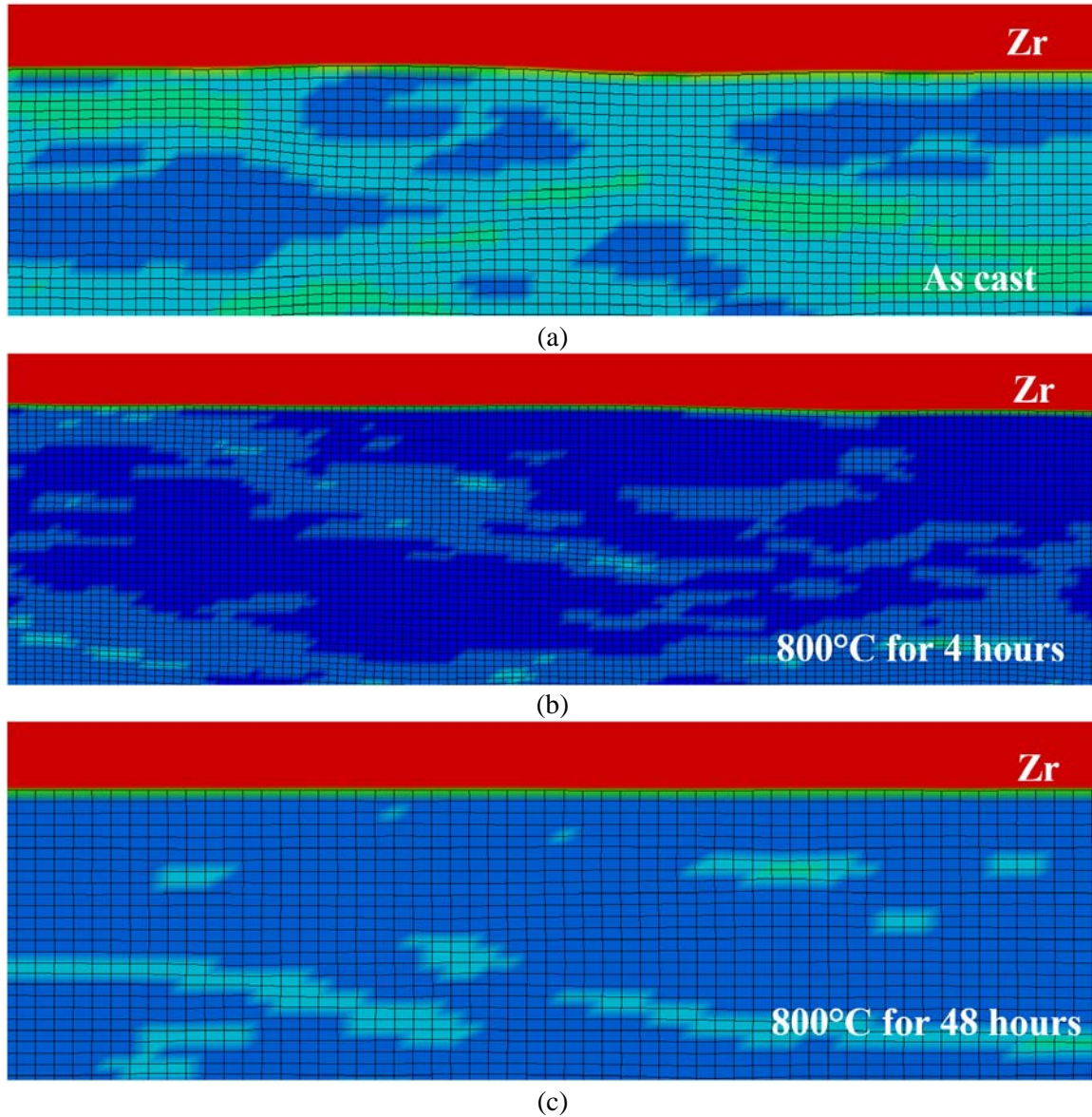


Figure 3.8. Compressive Loads on Zr (red) and U-10Mo Interface in Three Conditions:(a) As-Cast, (b) Homogenized at 800°C for 4 h, and (c) Homogenized at 800°C for 48 h

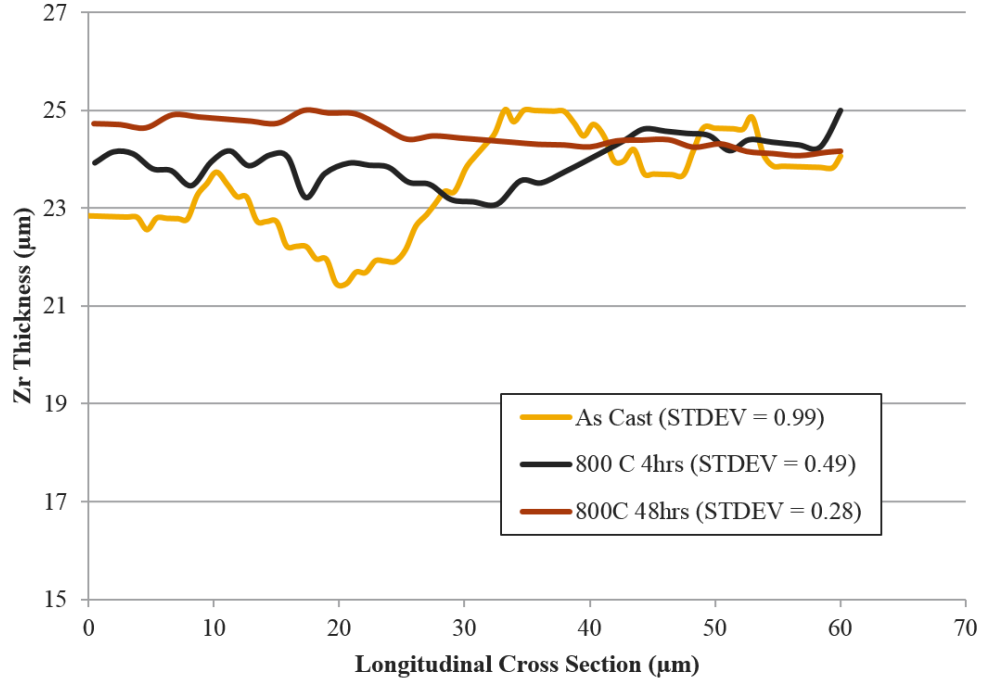


Figure 3.9. Zr Thickness Variation along Longitudinal Cross Sections

3.2.4 Tools Developed

3.2.4.1 Two-Point Correlation Functions

The purpose of the 2PCF is to quantify the spatial distribution of carbides during thermomechanical processing. For a two-phase material (matrix and particles in our case), the 2PCF is defined as shown in Torquato (2013) and Hu et al. (2018).

$$S_2^{(i)}(\mathbf{x}_1, \mathbf{x}_2) = \langle I^{(i)}(\mathbf{x}_1) I^{(i)}(\mathbf{x}_2) \rangle, \quad (3.1)$$

where I denotes the two phases ($i = 1, 2$), \mathbf{x}_1 and \mathbf{x}_2 are two randomly chosen points, $I^{(i)}(\mathbf{x})$ is an indicator function, and the angular brackets $\langle \dots \rangle$ denote ensemble averaging over the random medium. The indicator function $I^{(i)}(\mathbf{x})$ is defined as

$$I^{(i)}(\mathbf{x}) = \begin{cases} 1, & \mathbf{x} \in V_i, \\ 0, & \mathbf{x} \in \bar{V}_i, \end{cases} \quad (3.2)$$

where V_i represents the region of phase i , and \bar{V}_i is the region occupied by the other phase.

Consider a vector $\mathbf{r}^\theta = (r, \theta)$ with length r and angle θ randomly thrown into the microstructure as in Figure 3.10. The 2PCF in this study records the occurrence when each of two ends (\mathbf{x}_i and $\mathbf{x}_i + \mathbf{r}^\theta$) of the vector \mathbf{r} lands inside two different carbide particles using the following expression:

$$S_2^{(p)}(\mathbf{r}) = \sum_{i=1}^N I^{(p)}(\mathbf{x}_i) I^{(p)}(\mathbf{x}_i + \mathbf{r}) \quad (3.3)$$

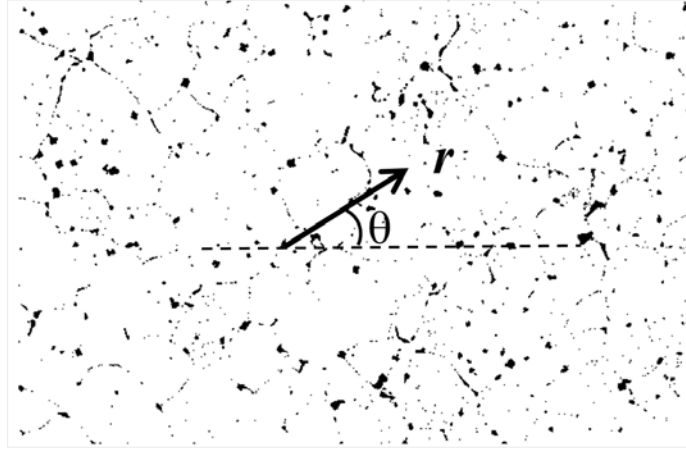


Figure 3.10. A Vector r with Length r and Angle θ in a Microstructure Domain

In Figure 3.10, the microstructure domains are elongated along the horizontal direction, yielding increased horizontal distance between particles after thickness reduction. In the through-thickness direction, the domains are compressed, and the particles become much closer to each other. To indicate the basic features of microstructures, the data output from the 2PCF analysis will be fed into the recrystallization and grain growth model.

Here, the as-cast initial microstructures generated from the homogenization model are considered for analysis of second-phase particle distribution resulting from rolling deformation. To elucidate the important aspects of carbon distribution upon rolling, the initial microstructure is directly mapped into the FEM plane-strain compression model and deformed to 20%, 40%, and 60% reduction of the original height. Figure 3.11(a) shows particle distribution over the domains after the rolling simulations. In the vertical direction (Figure 3.11(b)), it is evident that as the reduction increases from 0% to 60%, the 2PCF curves (i.e., $S_2^{(p)}(r, 90)$) shrink in the direction of the r axis, as the domain of analysis is reduced due to the thickness reduction. To provide sufficient data, the vertical direction is defined as a range of $\pm 15^\circ$ around $\theta = 90^\circ$. In the inset of Figure 3.11, the first peaks (square markers) represent the most probable nearest distance d_1 between particles, and the second peaks (triangle markers) represent the most probable second nearest distance, d_2 . As shown, both d_1 and d_2 decrease with rolling reduction. However, the change of the d_1 is quite small with reduction compared with changes of d_2 . This is expected, because particles usually appear in the form of clusters. The first peaks are mostly formed by the distances between particles inside each cluster, while the second peaks mostly represent the distances between particles from different clusters. During deformation, the changes in distances between different clusters are much larger than those inside each cluster. More examples and detailed discussion can be found in Hu et al. (2018).

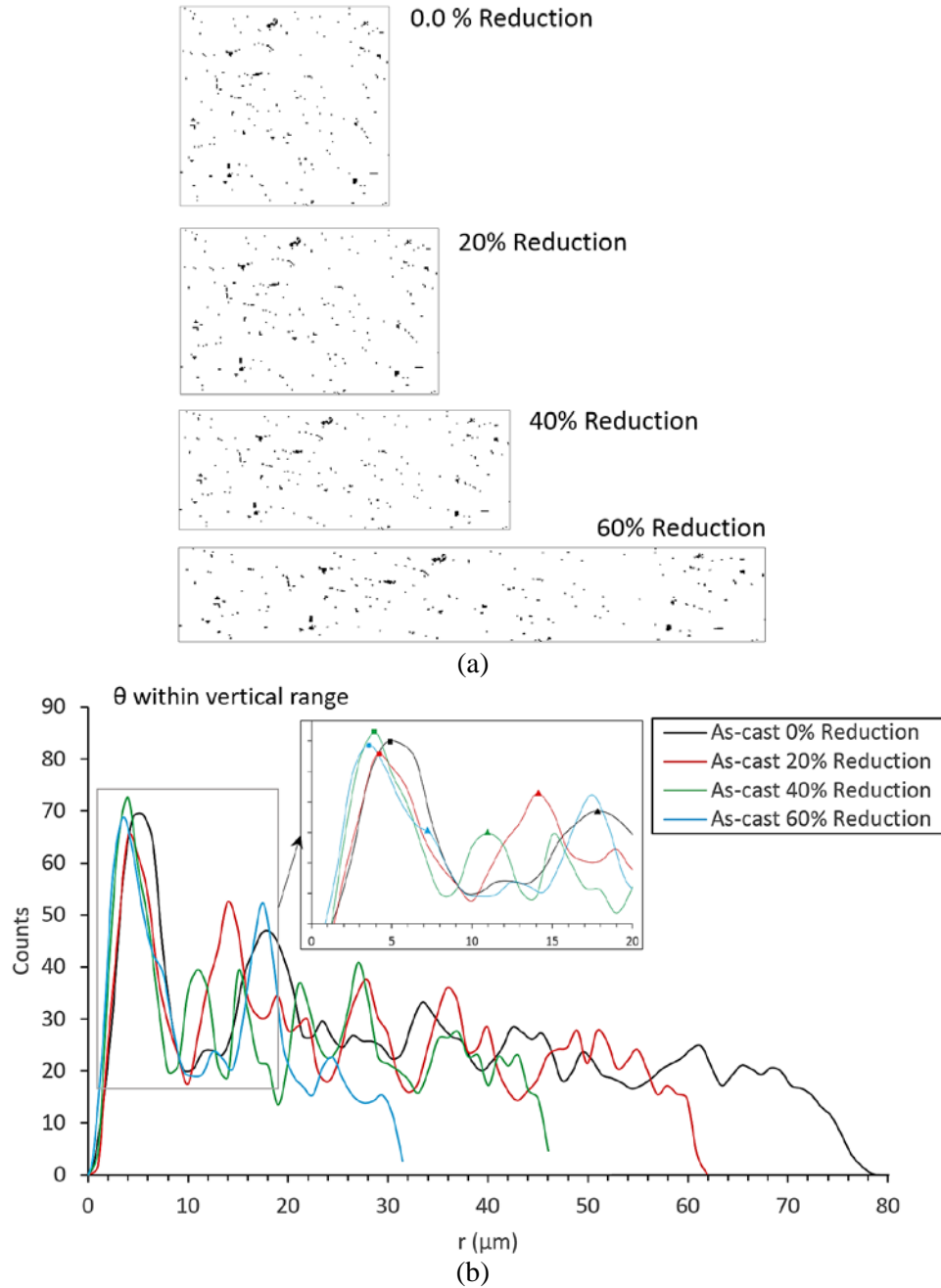


Figure 3.11. (a) Deformation Sequence of U-10Mo Microstructure; (b) Two-Point Correlation Functions along the Vertical Direction

3.2.4.2 Stringer Evolution during Hot-Rolling Reductions

Stringers or stringer-type particle clusters provide a possible propagation path for cracks or fractures, which lowers the damage resistance of the materials (Hannard et al. 2017). It is important to control the particles in the initial microstructures to obtain the desired material performance after hot rolling. To model stringers, each particle was approximated by an ellipse in the image analyses, as shown in Figure 3.12(a). A line was drawn to connect the center points of two particles, as shown in Figure 3.12(b). The angle between the connected line and the horizontal direction is defined as θ ; the line segments

within Particle 1 and Particle 2 and the distance between the two-particle centers are defined as r_1 , r_2 and d , respectively. The angles for angular misalignment between the particles were kept the same as specified in ASTM E45-05 at 10° . Because the critical distance between two particles was estimated as five times of the sum of two radii, the stringer identification criterion was defined as follows:

$$\theta \leq 10^\circ \quad (3.4)$$

$$d \leq 5 * (r_1 + r_2) \quad (3.5)$$

If two particles were found to satisfy the listed requirements, the particle pair was considered a two-particle stringer. Then, all the two-particle stringers were identified and a list of two-particle stringers and the particle labels was provided. Because one particle would be found in different two-particle stringer pairs, the obtained list was adjusted by merging two-particle stringers that included the same particle. Thus, a new stringer list, including three or more particles, was finally obtained and the SVF (the second-phase particle volume fraction in stringers) was calculated.

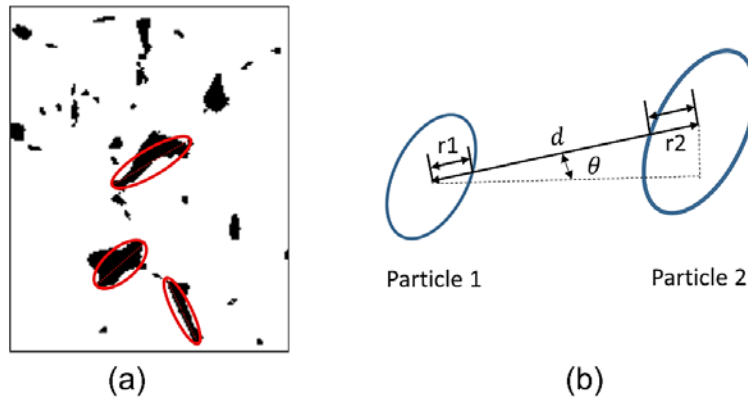


Figure 3.12. (a) Approximation of the Particles Using Ellipses and (b) Variables Used in Stringer Identification Criteria in this Study

Two different U-10Mo samples with varied second-phase particle concentrations, distributions, and sizes were used for this study. The details of the casting conditions and heat treatments are described elsewhere (Joshi et al. 2016; Xu et al. 2016; Nyberg et al. 2013). Their corresponding microstructures were observed under SEM, as shown in Figure 3.13. The grey regions are the individual U-10Mo grains and the dark spots are uranium carbide (UC) particles. The volume fractions, sizes, morphologies, and distributions of UCs are quite different among samples because of the different annealing processing parameters and compositions of the samples.

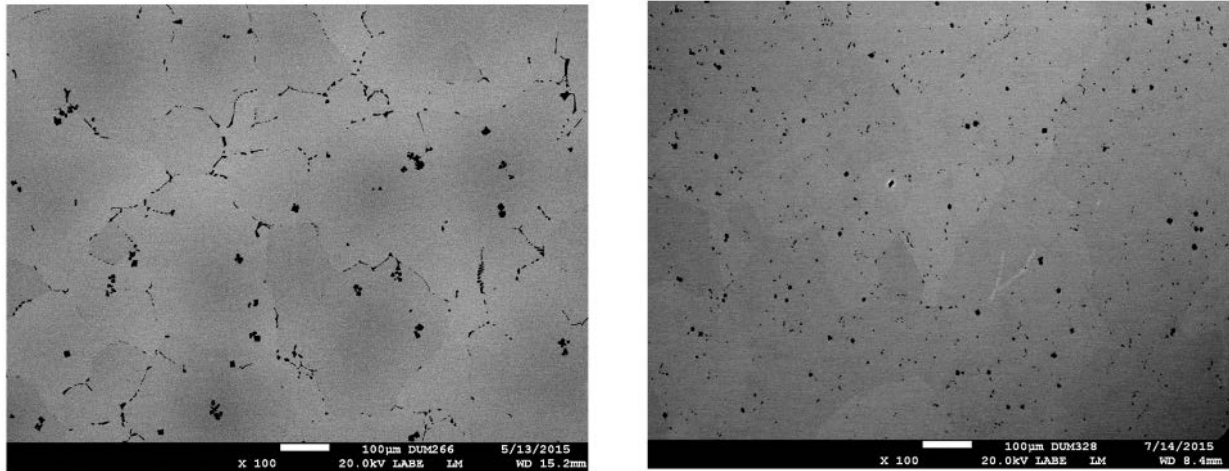
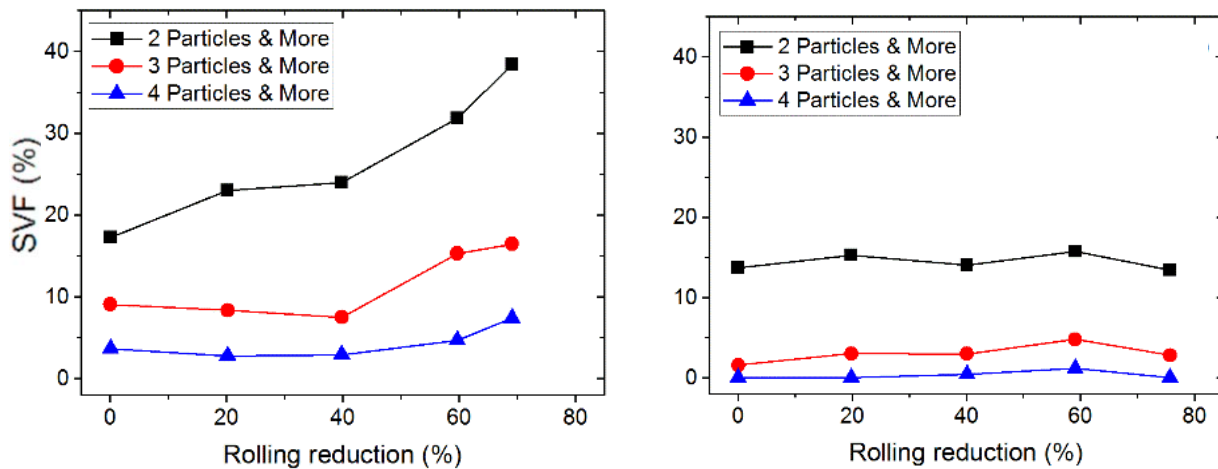


Figure 3.13. SEM Images of Initial Microstructures for Two Samples: (a) Particles Distributed along Grain Boundaries; (b) Randomly Distributed Particles

The correlations between SVFs and the rolling reductions of two samples are summarized in Figure 3.14. The correlation between SVFs (i.e., two-particle stringers and three-particle stringers) and rolling reduction were found to be quite different among samples for which the rolling reduction rate increased to over 70%, because each sample had a unique particle volume fraction (PVF), particle size, and particle distribution (i.e., particle spacing). The particle distribution and morphologies affected SVF evolution quite significantly. Samples with initial carbides distributed along grain boundaries (Figure 3.13(a)) exhibited high SVFs. Many high-particle-number stringers were identified. In the initial microstructures, high-aspect-ratio particles were aligned along the grain boundaries. After rolling reduction, these high-aspect-ratio particles were rotated and the long axes of these particles were aligned along the rolling direction. The current stringer identifications are based on the distance between the two particles, so these high-aspect-ratio particles could easily be associated with neighboring particles and constitute a high-particle-number stringer (i.e., three-particle stringer or four-particle stringer, as the red and blue symbols denote, respectively). In Figure 3.13(a), the particles along grain boundaries were more numerous and few randomly distributed particles could be observed. Thus, the SVF increased much faster with rolling reduction. In contrast, the sample with randomly distributed particles (Figure 3.13(b)) would not show an SVF increase with rolling reduction. Also, fewer three-particle stringers were observed. High-aspect-ratio-particles were rarely observed in the initial microstructures, and most particles could be approximated by a circle. The rotation of these circular particles did not affect the stringer identification criterion significantly. Thus, SVF increases were not observed, and few high-particle-number stringers existed for this sample. More examples and detailed analysis can be found in Cheng et al. (2018).



(a) (b)

Figure 3.14. SVF vs. Rolling Reduction for Two Samples: (a) Particles Distributed Along Grain Boundaries, (b) Randomly Distributed Particles

3.2.4.3 Carbide Particle Redistribution

The developed carbide particle redistribution toolset allows users to analyze maximum stringer length and number of near-surface carbide particles for any given microstructure. Some examples and associated findings are listed below. The details can be found in Choi et al. (2018). First, maximum stringer length can be higher with higher PVFs. Maximum stringer length substantially increases with increased rolling reduction (by about 30~50% for the 40~80% rolling reduction) for the microstructures with elliptical particles along grain boundaries (as shown in Figure 3.15(a)). For other microstructural features (i.e., random particle distribution with circular/elliptical particles, and particle distribution along grain boundaries with circular particles), as shown in Figure 3.15(b, c, and d), the increase of maximum stringer length with rolling reduction is less significant (by about 5~30% for the 40~80% rolling reduction). The reason for studying the carbide particles distributed randomly and along grain boundaries is that both of the scenarios are observed in the SEM images.

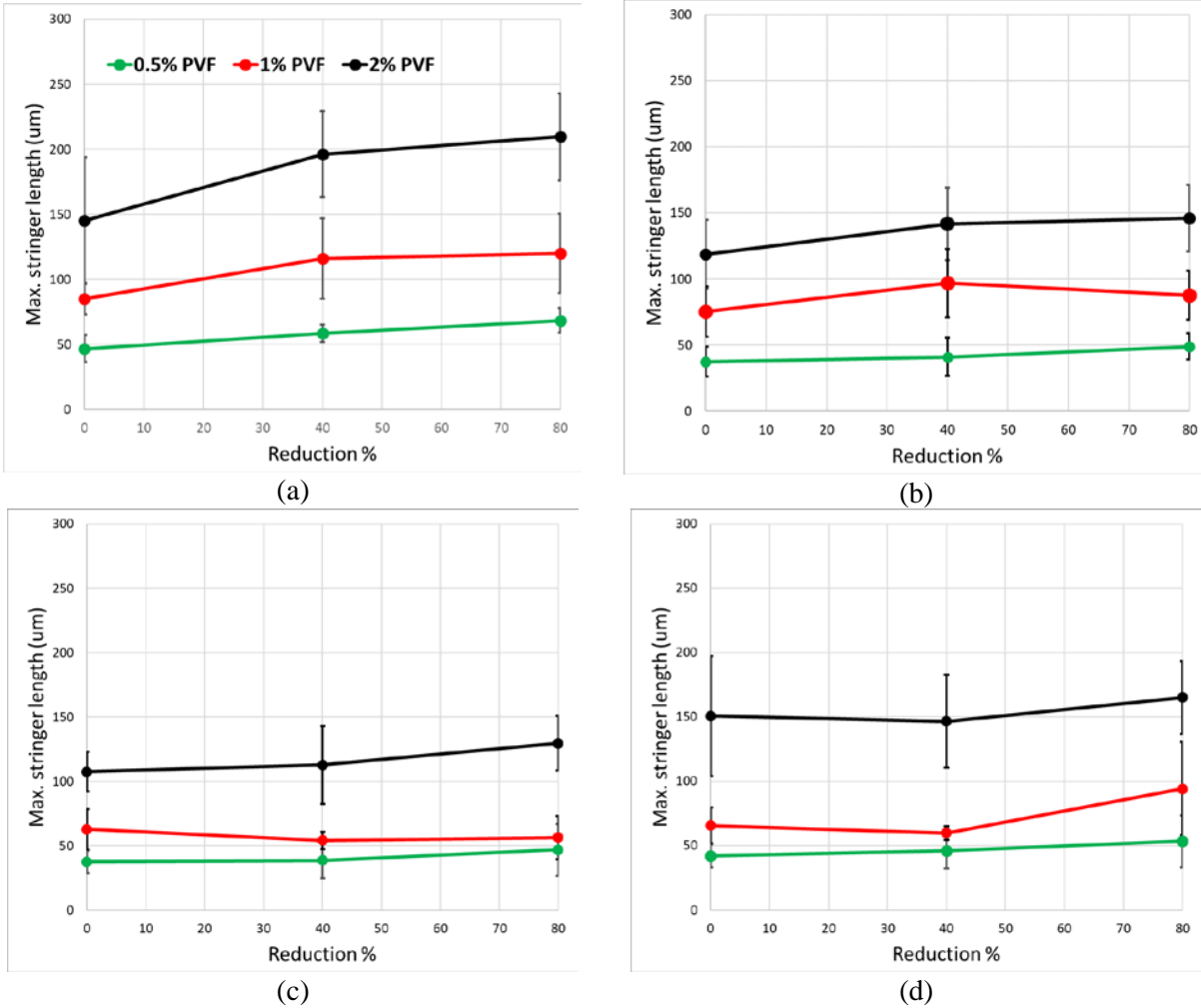


Figure 3.15. Maximum Stringer Length for (a) Elliptical Particles Distributed along Grain Boundaries; (b) Circular Particles Distributed along Grain Boundaries; (c) Randomly Distributed Circular Particles; (d) Randomly Distributed Elliptical Particles

Next, the evolution of particle distributions near the surface was investigated, because carbide particles near the surface can influence the fuel quality and stability. Figure 3.16 presents a way to obtain the near-surface particle information. As shown in the figure, a depth of 70 μm from the surface was arbitrarily selected to represent near-surface depth, and the same value was used in the deformed microstructures after 40% and 80% rolling reductions. There was with no noticeable difference between results for the microstructures with circular particles and those with elliptical particles, so only the results for the circular particles are presented here. The calculations were performed for both the top and bottom surfaces of all the generated microstructures. The numbers of near-surface particles increase by $\sim 80\%$ and $\sim 550\%$ with the 40% and 80% rolling reductions, respectively, as shown in Figure 3.17(a). Near-surface PVF prior to rolling may be different from the given overall PVF. With increased rolling reduction, near-surface PVF can increase slightly and approach the given overall PVF, as shown in Figure 3.17(b). Note that the total PVFs increase by $\sim 5\%$ and $\sim 15\%$ from the initial PVF with the 40% and 80% rolling reductions, respectively. This is probably due to a slight increase of PVF that may have been introduced in error during the remeshing process after each rolling simulation. Therefore, the results in Figure 3.17(b) are to be analyzed with these errors considered.

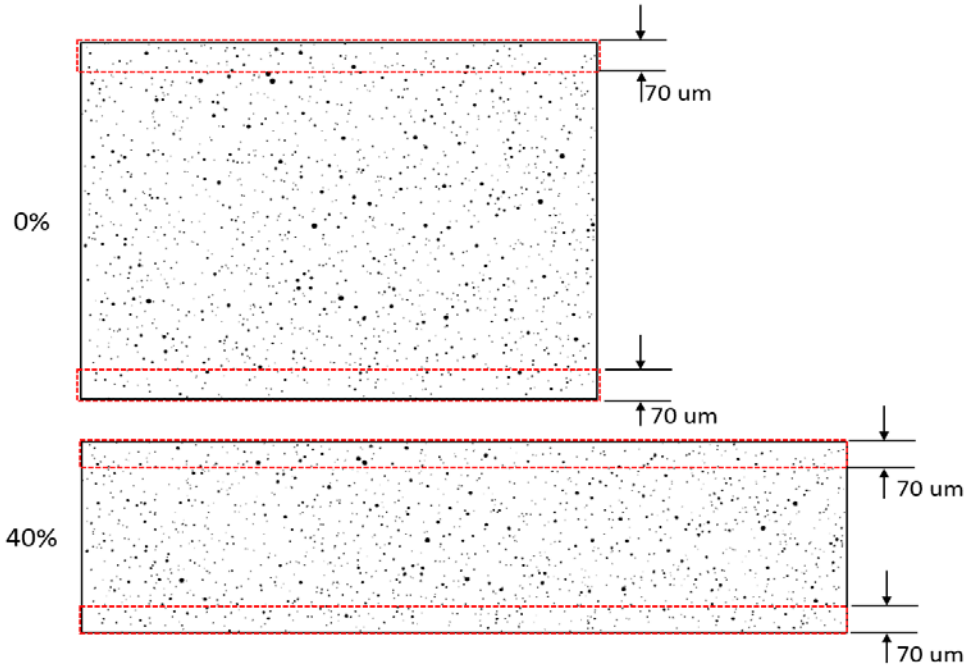


Figure 3.16. Schematics for Near-Surface Particle Information. This model shows random particle distribution with 2% PVF.

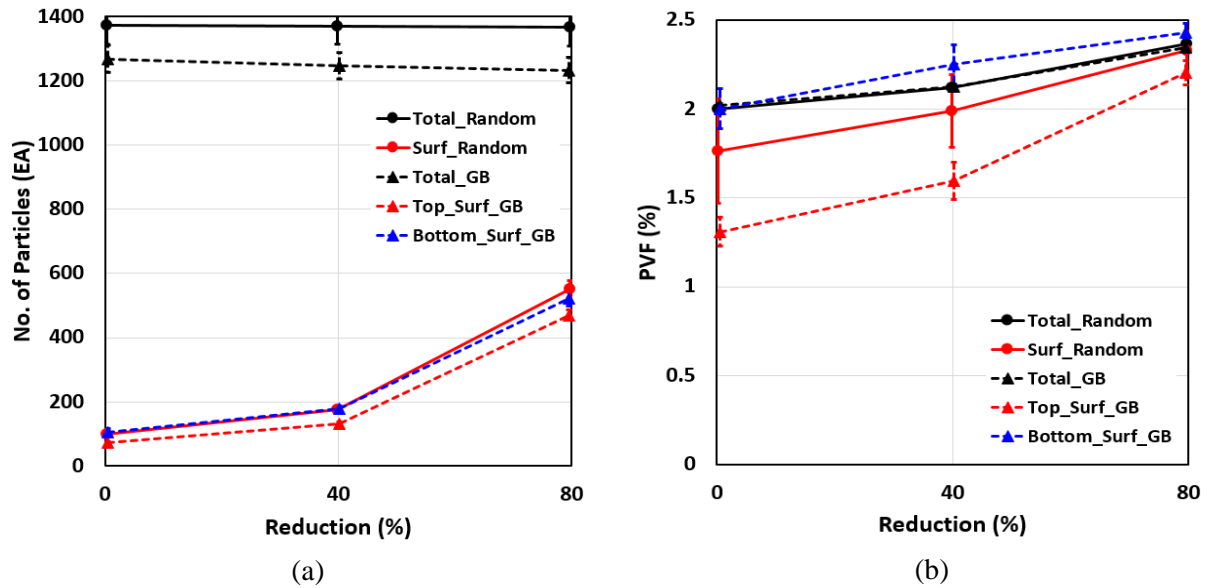


Figure 3.17. Evolution of Near-Surface Number of Particles and PVF during Rolling: (a) Number of Near-Surface Particles for the Microstructure Shown in Figure 3.16; (b) Near-Surface PVF. GB is grain boundary.

4.0 Annealing

4.1 Model Description

Grain growth and recrystallization simulation uses the Potts model of grain growth, a Q-state generalization of the Ising Model (Potts and Ward 1955). The Potts model has previously been used to simulate a variety of microstructural phenomena, such as abnormal grain growth, recrystallization, grain growth in the presence of grain boundary energy and mobility anisotropy, subgrain coalescence, particle pinning, and void coarsening (Rollett et al. 1989, 1992; Tikare and Cawley 1998a, b; Tikare and Holm 1998; Holm et al. 2003, 2015; Park et al. 2012; Frazier et al. 2015; Williamson and Delplanque 2016). The simplest version of the Potts model works in the following way: a grid of grain orientation IDs, or “spins,” usually constituting a hexagonal or cubic lattice, is generated. The initial grid can generate IDs for each cell in the grid either by using an existing microstructure or by picking the IDs randomly. The simulation then allows reorientations of the grain IDs based on the energetics of the reorientations. The energy of the entire system is described as

$$E = \frac{J}{2} \sum_i^N \sum_j^{NN} (1 - \delta_{s_i s_j}) \quad 4.1$$

Here, the energy of the system E is dependent on the internal energy of each cell in the grid, U_i , and on the interaction energy of each cell in the grid with unlike nearest, next-nearest, and next-next-nearest neighbors, J . The term δ represents the Kronecker delta function. The probability of reorientation at a specific lattice site is then

$$p = \begin{cases} \frac{M_{ij} \gamma_{ij}}{M_{max} \gamma_{max}} & \Delta E \leq 0 \\ \frac{M_{ij} \gamma_{ij}}{M_{max} \gamma_{max}} e^{-\frac{\Delta E}{T_s}} & \Delta E > 0 \end{cases} \quad 4.2$$

Here, ΔE is the change in the system energy associated with the reorientation, M_{ij} is the mobility of the reorientation, M_{max} is the maximum mobility of a reorientation, and T_s is the nonphysical simulation temperature, which is used to prevent the simulation lattice from pinning grain boundaries (Zöllner 2014). The relative mobilities of these orientations as affected by temperature can be calculated using the methods described by Safran et al. (1983) and Raabe (2000).

4.1.1 Integration with FEM Rolling Model

The internal energy of each cell in the grid, U_i , is used to account for the deformation energy from rolling in Equation (4.1). This deformation energy can be calculated directly from strain data by integrating over the U-Mo stress-strain curve. FEM simulates deformation well for a given microstructure, can account for complex constitutive relationships in deformation, and is well equipped to produce these data for Potts model simulations. The coupling between the FEM model and the Potts model in this particular execution effectively parallels the U-Mo rolling process, in which the fuel meat iteratively passes through rollers and then undergoes annealing. Integrating the FEM model and the Potts model simulations in this way enables the simulation of microstructural evolution during complicated materials processes where large deformations and recrystallization occur.

This integration was done through an iterative process for the multiple passes during the rolling process, which required two-way information passing between the two models. The deformation output (stress, strain, and strain energy density) from the FEM model was supplied to the recrystallization model through the energy term. The simulated microstructure from the recrystallization model provided the texture information to the next round of FEM analysis. The strains calculated by FEM simulation are shown in Figure 4.1.

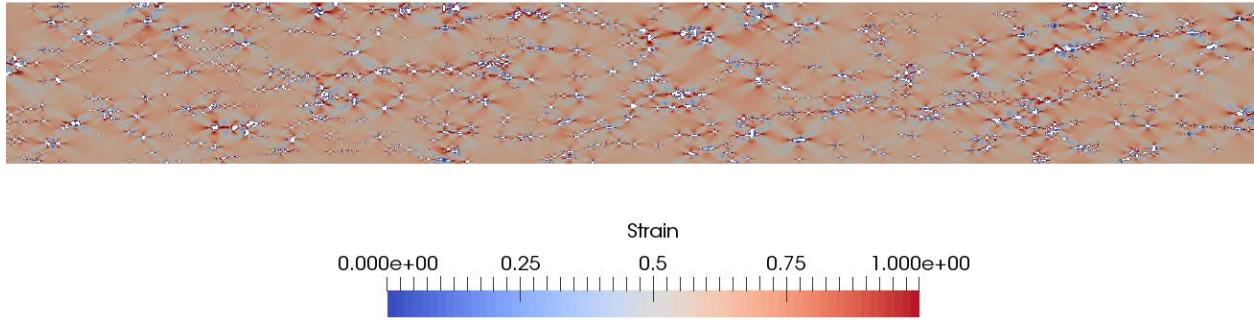


Figure 4.1. Strain from an FEM Simulation of Rolling to 65% Reduction, used as Input for the Potts Model Simulation of Recrystallization. Particles within the microstructure appear white.

We can use the abovementioned methodology to simulate recrystallization and grain growth in an entire microstructure. If the FEM model and the Potts model use identical cellular lattices, it is simple to use particle locations from a micrograph, 3D microstructure, or simulated microstructure in the Potts model. In these cases, the particle cells simply map to the initial microstructure in the Potts model. If the Potts model lattice is not the same as the input lattice, then the representation of the initial microstructure in the Potts model lattice becomes less exact. For example, FEM simulations simulate deformation through the use of an unstructured mesh, and do not perform simulations on a cellular lattice. In order to integrate FEM simulations from the previous section of this work properly, we can use a spatial interpolation algorithm to translate the FEM model output to a cellular lattice for the Potts model input.

This approach was used to demonstrate the simulation of recrystallization during multiple rolling passes. This recrystallization information was used to study different factors that are expected to influence recrystallization, such as reduction percentage and the distribution of particles within the microstructure. As we will show, these can have significant effects on the recrystallized microstructure and recrystallization kinetics.

4.2 Model Validation

Using appropriate simulation parameters, the simulations can reproduce the recrystallization behavior experimentally observed in multiple-pass hot rolling. In this work, a set of simulations was performed first to establish that the static recrystallization kinetics predicted were in reasonable agreement with experiments. FEM simulations were performed on a polycrystalline grain structure captured from an EBSD micrograph, as shown in Figure 4.2.

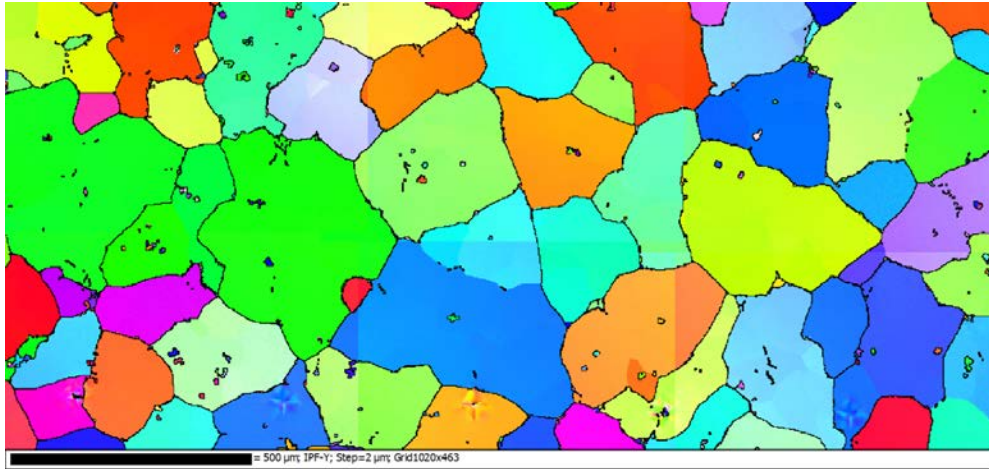


Figure 4.2. The Initial U-10Mo Microstructure, as Captured by EBSD

Next, a set of simulations was run performing multiple hot-rolling passes in 15% reductions, with an equivalent of 20 minutes of annealing at 700°C simulated in the Potts model after each pass. The resultant microstructures are shown alongside the experimentally observed microstructures for the equivalent treatments in Figure 4.3. The two sets of microstructures appear reasonably similar. After a single rolling and annealing pass, there is some recrystallization along the areas that have experienced the most strain. After the second rolling pass, additional recrystallization occurs, and more fine recrystallized grains appear. Several large grains from the as-rolled microstructure remain. By the third rolling and annealing pass—a total of 45% reduction in thickness from the original fuel foil and an hour total of annealing—the fine, recrystallized grains now compose a majority of the remaining microstructure, with a small population of grains from the initial grain structure remaining.

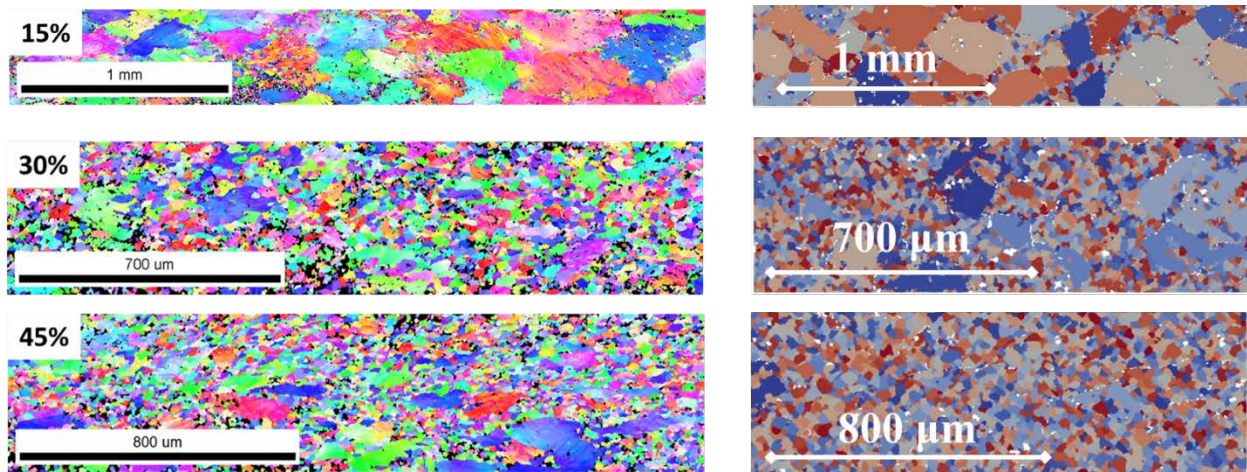


Figure 4.3. The U-10Mo Microstructure after One (15%), Two (30%), and Three (45%) Hot-Rolling Passes and 20-Minute Intermediate Anneals at 700°C, as Observed Experimentally with EBSD (left), and in Potts Model Simulation (right). Second-phase particles in the Potts Model simulations appear in white.

Continuing these simulations for an additional 15% and 18% reduction, for a total reduction of 78%, the Potts model was run to predict the recrystallization response upon annealing at 600°C and at 700°C. A

comparison between the experimentally observed recrystallization kinetics and the simulated behavior is shown in Figure 4.4. Simulation and experiment in this case appear to show reasonable agreement.

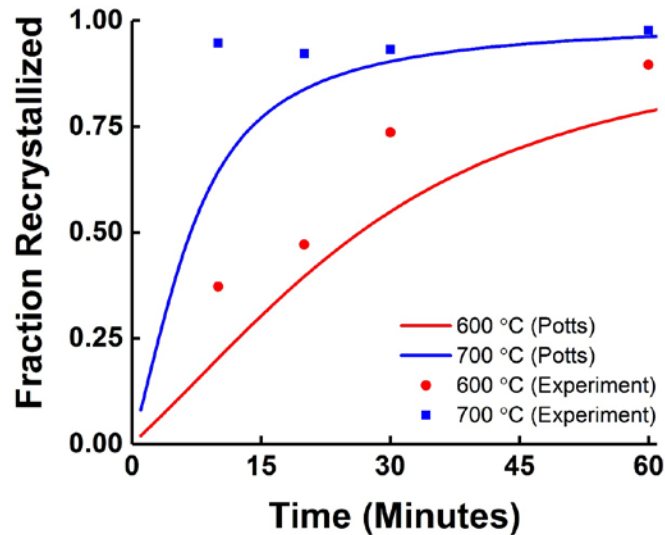


Figure 4.4. The Recrystallization Progress of 78% Hot Rolled U-10Mo after annealing at 600°C and 700°C, as Predicted by the Potts Model, for Five Passes with 20-Minute Intermediate Anneals at 700°C. Experimentally observed recrystallization progress for 80% hot rolled U-10Mo is shown for comparison.

A comparison between the experimentally observed grain size distributions and those from each reduction in our simulations confirm that the simulation predictions are reasonable, as can be seen in Figure 4.5. In both simulation and experiment, the recrystallized grains reach an average diameter of approximately 20 μm . The size distributions have long tails, which constitute older, deformed microstructure. The length of this tail in the grain size distribution visibly decreases with additional annealing passes.

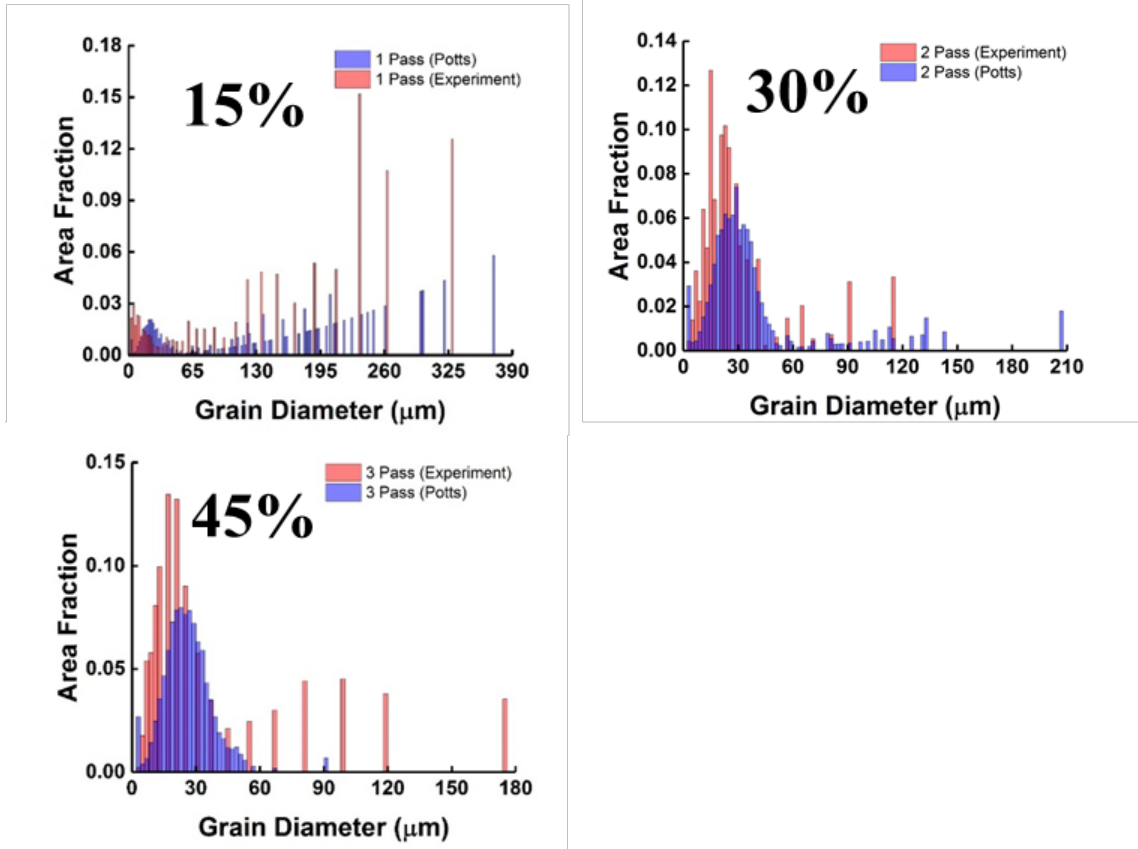


Figure 4.5. The Grain Size Distribution of U-10Mo for One to Three Passes of 15% Rolling Reduction and 20 Minutes of Annealing at 700°C, Up to a Total of 45% Reduction in Thickness and 60 Minutes Annealing. Histograms comparing experiment and simulation.

4.3 Impact for Program

Our model can evaluate the deformation and recrystallization behavior for any combination of rolling and annealing treatment. This can be used to evaluate the differences between reduction through multiple passes vs. single rolling passes, and devise a desirable rolling and annealing routine. In order to demonstrate this capability, a 45% rolling reduction was performed on the same microstructure, and an hour of annealing at 700°C was simulated in the Potts model, which is the equivalent cumulative deformation and annealing treatment to our multiple-pass simulations. These simulations show noticeably different recrystallization kinetics, as shown in Figure 4.6(b). Specifically, recrystallization occurs much more rapidly after a direct rolling pass. A comparison between the strain distributions from the three-step rolling and the direct pass shows that the accumulated strain in the microstructure is more significant for a direct pass, as shown in Figure 4.6(a).

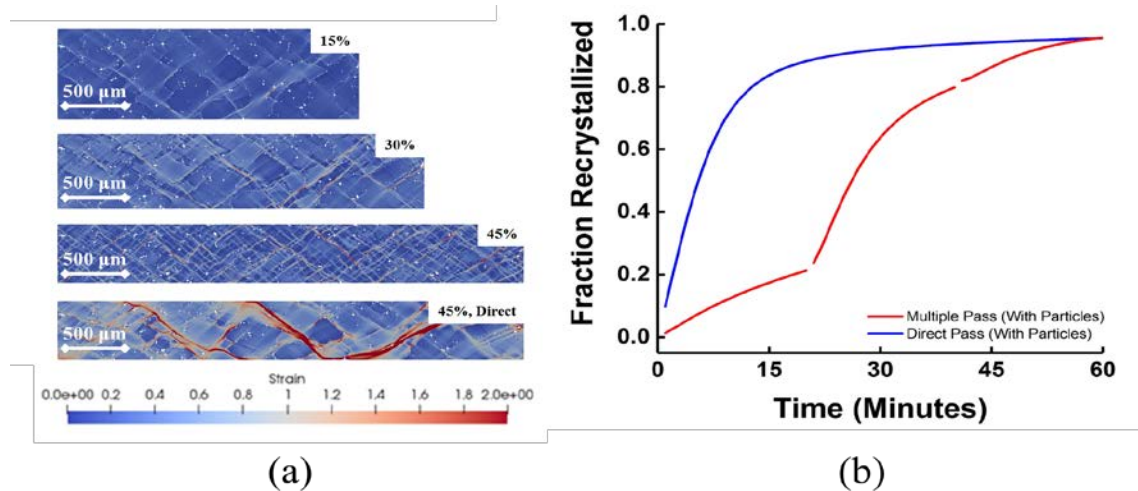


Figure 4.6. (a) The Strain Distribution of U-10Mo for Hot-Rolling Reductions of 15%, 30%, and 45% with Intermediate Annealing Steps, Compared with the Strain Distribution of U-10Mo for a Single Hot-Rolling Pass to 45%. Second-phase particles are shown in white. (b) The Recrystallization Progress of U-10Mo as Predicted by the Potts Model for a Single Hot-Rolling Pass with 45% Reduction and for Three 15% Hot-Rolling Passes with Intermediate 20-Minute Annealing Steps. All anneals were performed at 700°C.

While we still must account for factors not considered in this implementation of our model, such as the presence of fine particles that suppress grain growth, our method gives us extensive freedom in the rolling and annealing treatments we can consider.

4.4 Tools Developed

We have developed a method to predict the microstructure of LEU-Mo fuel after multiple passes of rolling and heat treatment. We have demonstrated that this prediction can be achieved with reasonable accuracy given the initial U-10Mo microstructure and the deformation and annealing treatments to be evaluated. With this information, our simulations can predict numerous key features of the foil microstructure that affect fuel processing and performance, as described in Table 4.1.

Table 4.1. Microstructural Information and its Significance in Fuel Processing/Performance

Microstructural Information	Significance
Average Grain Size	Foil Strength, Irradiation Resistance
Grain Size Distribution	Foil Strength, Irradiation Resistance, Zr-Layer Effects in Processing (Orange Peeling)
Spatial Variations in Grain Size Distribution	Foil Strength, Irradiation Resistance, Zr-Layer Effects in Processing (Orange Peeling)
Recrystallization Kinetics	Controls Annealing Time/Processing Temperatures Required
Extent of Particle Stimulated Nucleation (PSN)	Controls Annealing Time/Processing Temperatures Required, Controls Grain Size, Dependent on Homogenization Parameters

5.0 Cold Rolling

5.1 Macro-FEM Model

5.1.1 Model Description

The cold-rolling model is very similar to the hot-rolling FEM model described previously. No lubricant was used and rolling passes were conducted at room temperature. The previously developed FEA model was used to conduct the simulations. The U-10Mo behavior was described using an elastic-plastic constitutive model with the material yield stress of 780 MPa and an ultimate tensile stress of 1100 MPa. Friction between the U-10Mo sample and the rolls was modeled using a Coulomb friction coefficient of 0.1. Higher friction coefficients were also used, and parametric study results will be reported in detail. The rolls are made of H13 steel. Only the elasticity of the rolls was considered, with no vertical displacement allowed. U-10Mo mechanical properties at room temperature were used to define its behavior. Simulations were conducted to study the effect of roll diameter on ability to attain desired U-Mo gage/thickness, produce uniform through-thickness strain, and achieve an effective roll-separation force and the torque required to properly roll foils. This model investigated rolls with 0.5", 7/8", 1.25", 2", and 3.75" working-roll diameters.

5.1.2 Model Validation

The model was validated through comparison of the predicted roll-separating forces with the experimental measurements made using PNNL's rolling mill with 7/8" and 1.25" rolls on a ~1" wide bare foil. Table 5.1 presents a comparison between the predicted (simulation) and measured (experimental) roll-separation forces for different reductions using PNNL's 1.25" and 7/8" diameter rolls.

Table 5.1. Predicted and Measured Roll-Separation Force (RSF)

Pass#	Reduction	Exp. RSF	Sim. RSF	Reduction	Exp. RSF	Sim. RSF
		(lbf) 7/8"	(lbf)		(lbf) 1.25"	(lbf)
1	8.6%	9,300	9,697	10%	11,200	12,498
2	10.76%	10,180	11,053	15%	12,500	13,210
3	14.57%	10,020	12,006	15%	12,500	13,805
4	11.76%	10,400	11,789	15%	13,500	14,458
5	20%	11,800	12,687	25%	14,000	15,298

Predictions and measurements were in good agreement, which gave us confidence in the model's ability to predict the behavior of rolled U-10Mo using rolls with different diameters, different lubrication, and different tensioning.

5.1.3 Impact for Program

The model clearly showed that reducing the roll diameter helps decrease the difference between desired and actual foil thickness. The model also showed that the 3.75" diameter roll is not able to roll the sample

below 0.011” without preloading of the sample (even under ideal conditions). With the 7/8” and the 1.25” rolls, it was easier to attain the desired thickness at reduced loads, and thus these thicknesses have been recommended. The desired mill specifications, with roll diameter between 7/8” and 1.25”, and improvement in the cold-rolling schedule was also established and communicated to BWXT.

The model can be used to predict the effects of tensioning, roll diameter, and reductions on the ability of the rolling mill to achieve the desired thickness.

Table 5.2 below shows model predictions of the minimum achievable thicknesses at 10% and 30% per pass for different roll diameters. Smaller rolls, 7/8” and 1.25”, were able to achieve 0.01” thickness, whereas 2” and 3.75” rolls were not able to roll the sample thinner than 0.02”. These results are in agreement with the theoretical equations calculating the minimum thickness as a function of roll diameter, material, and friction.

Table 5.2. Predicted Achievable Thicknesses

Starting Thickness	10% Reduction				30% Reduction			
	7/8” Roll	1.25” Roll	2.0” Roll	3.75” Roll	7/8” Roll	1.25” Roll	2.0” Roll	3.75” Roll
0.04”	✓	✓	✓	✓	✓	✓	✓	✓
0.03”	✓	✓	✓	✓	✓	✓	✓	✓
0.02”	✓	✓	✓	✗	✓	✓	✗	✗
0.01”	✓	✓	✗	✗	✓	✓	✗	✗

Simulations were also performed to measure the roll-separation force as a function of passes/thickness. It can be observed from Figure 5.1 that the load separation force is proportional to the square root of the radius of the working rolls. Thus, the smaller the rolls, the lower is the roll-separation force. Similar data for 10%, 20%, and 40% reduction are also available and can be found in a separate cold-rolling report (in preparation). The torque values were also calculated for the same and similar trends to the load separation forces (not shown).

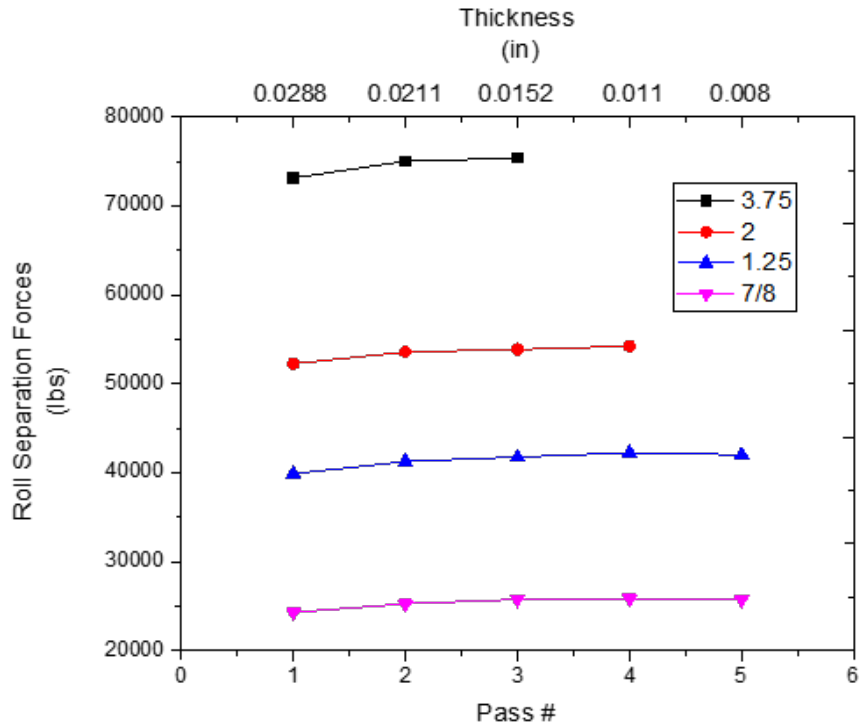


Figure 5.1. Predicted Roll-Separation Force as a Function of Number of Passes and Sample Exit Thickness using Different Roll Diameters

Figure 5.2 presents parametric study results of cold-rolling simulations using a BWXT 3.75” diameter mill. Roll-separating force simulations were conducted using a 0.3 friction coefficient and a 10% reduction. The roll-separating force clearly increased with sample width and thickness. These results can be used as guidance for sample and rolling designs.

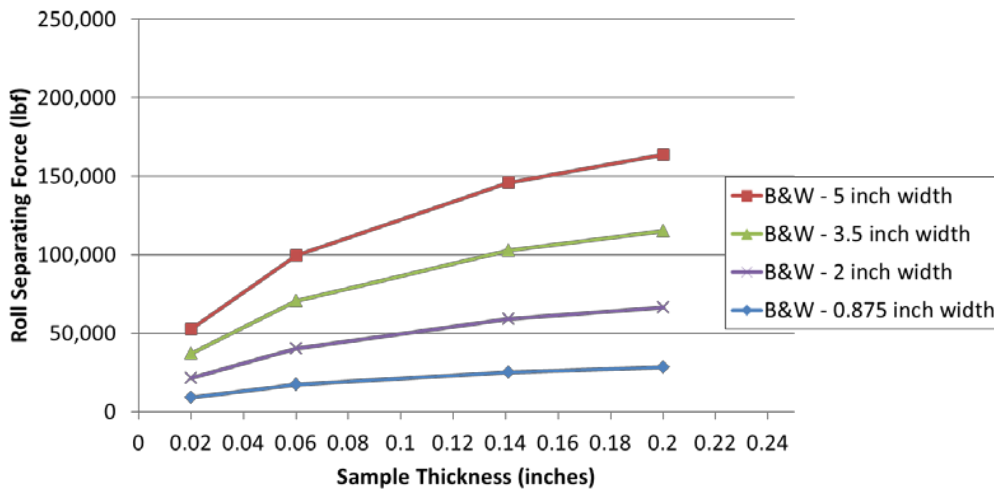


Figure 5.2. Predicted Roll-Separating Force as a Function of Thickness for Four Different Sample Widths at a 0.3 Friction Coefficient for the BWXT Cold-Rolling Mill

5.1.4 Tools Developed

A multipass cold-rolling FEA model was developed in LS-DYNA. The model can simulate the effect of roll diameter, U-10Mo sample geometry, can material and geometry, rolling speed, and temperature.

5.2 Microstructure-Based FEM Model

5.2.1 Model Description

2D plane-strain compression modeling was applied to simulate hard particle fracture in cold rolling. The boundary conditions were same as those previously used for the hot-rolling simulation. However, the input properties were different regarding the temperature and the fracture behaviors of second-phase particles. The room temperature properties of the matrix material, which were used for the cold-rolling model, were based on the results of Burkes et al. (2009b) of U-xMo material deformed at room temperature (see Figure 5.3).

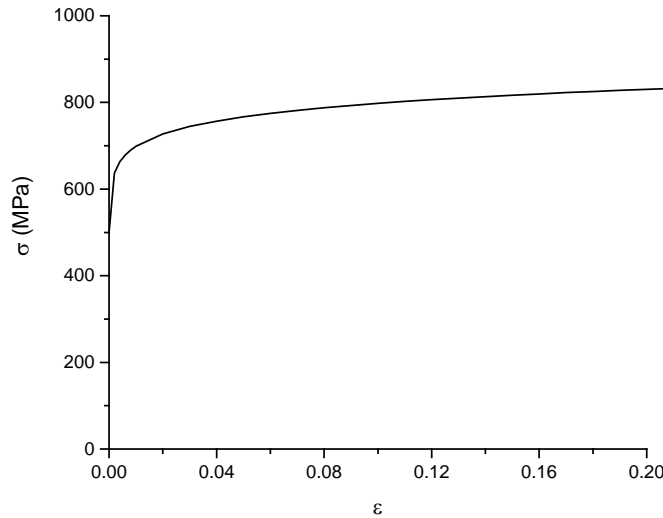


Figure 5.3. Flow Curve of U-10Mo Matrix Material at Room Temperature

During cold rolling, the UC particles experience much higher stresses than during hot rolling, and second-phase particle fracture is often observed. Because the carbide is a brittle material and does not deform plastically during rolling, its fracture is mainly stress induced. In the current work, a tension failure model is used for the criterion of particle fracture, i.e., the particle will fracture after the hydrostatic tensile stresses (σ_h) reach a critical value (σ_c):

$$\sigma_h = \frac{1}{3}(\sigma_1 + \sigma_2 + \sigma_3) = \sigma_c \quad (5.1)$$

In the current work, the critical stress is assumed to be 900 MPa.

5.2.2 Model Validation

The cold-rolling simulation was performed based on a portion of the microstructure of previously hot rolled U-10Mo sheet. The microstructure was pixel-mapped into the Abaqus/Explicit plane-strain compression model, as shown in Figure 5.4. The plane-strain compression model representing cold rolling has boundary conditions identical to those for hot rolling, but different material properties, as discussed earlier. In addition, a fracture criterion has been added into the model.

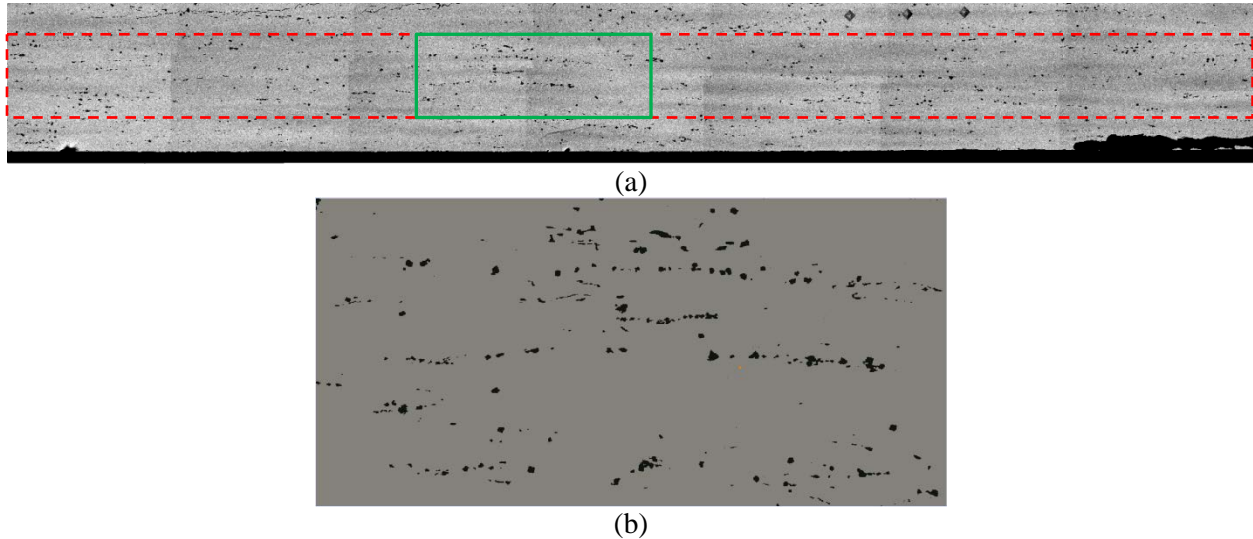


Figure 5.4. The Finite-Element Cold-Rolling Model: (a) Micrograph; (b) Modeled Portion of the Region Marked with a Green Rectangle in (a)

Here only one cold-rolling reduction of 25% is attempted. The simulated microstructure after cold-rolling reduction of 25% is shown in Figure 5.5(a). Features with white color are areas where the material fracture criterion is reached for carbide particles, and elements are removed from the model. These features can be deemed cracks, which can be compared with experimental observations as shown in Figure 5.5(b).

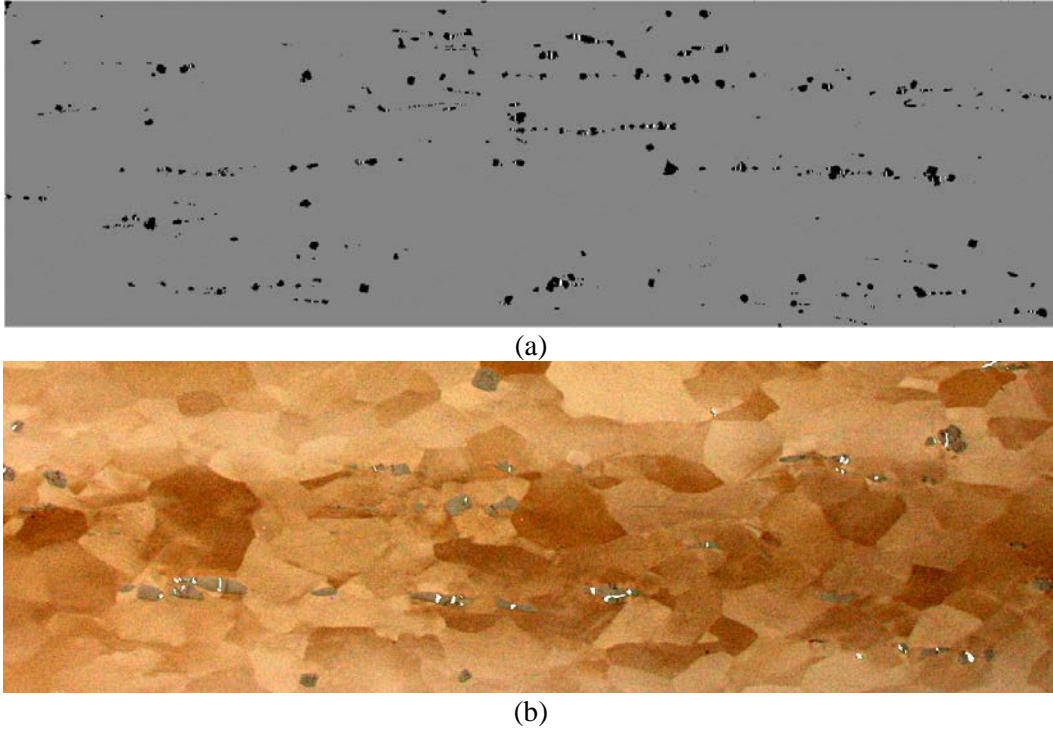


Figure 5.5. Simulated Particle Fracture (a) in Comparison with Experimental Microstructure (b)

Comparing Figure 5.5 (a) and (b) shows that the simulated result is qualitatively similar to that observed experimentally. In the simulated microstructure, the particle volume fraction is 1.78%, and the void volume fraction generated during cold rolling is $\sim 0.11\%$ of the entire area. In the actual microstructure, the particle volume fraction is 1.98%, and the void volume fraction generated during cold rolling is $\sim 0.15\%$ of the entire area. Also, most of the voids generated among the particles are perpendicular to the rolling directions, as shown in both the experimental and simulated results. The similarities in void volume fraction and fracture behaviors demonstrated that the current simulation setup could predict second-phase particle fracture during cold rolling with a small error. Future study, including grain orientations (Hu et al. 2008) and different grain flow stress (Cheng et al. 2016a,b) will provide more accurate predictions.

5.2.3 Impact for Program

The FEM model developed for simulating the cold-rolling process can be used to characterize the carbide fracture and identify the impact of defects and their locations on downstream processing. Meanwhile, the computational method can also be used to determine the optimal rolling schedule, which can help reduce the fabrication cost.

5.2.4 Tools Developed

A finite-element simulation framework was developed based on Abaqus. The developed simulation tools can mimic the material deformation and particle fracture during the cold-rolling process. The microstructure evolution during the rolling process can also be captured. The cold-rolling simulation is designed to fine-tune the material to the desired thickness.

6.0 Post-Cold-Rolling Recrystallization

6.1 Model Description

The recrystallization process typically exhibits Arrhenius-like behavior with respect to temperature and its activation energy, so the activation energy of recrystallization after cold rolling can be calculated using the following equation:

$$\frac{\tau_1}{\tau_2} = e^{\frac{-Q}{R} \left(\frac{1}{T_2} - \frac{1}{T_1} \right)} \quad 6.1$$

Here, τ_1 and τ_2 denote the time required to reach 50% recrystallization of the microstructure at two different temperatures, T_1 and T_2 . The term Q denotes the activation energy for recrystallization, and R is the universal gas constant.

Along with the activation energy of grain growth, the activation energy of recrystallization of U-10Mo is important for modeling and simulating its grain structure evolution. This parameter determines the rate of recrystallized grain nucleation as a function of time and temperature, and can be used as direct input for recrystallization simulations (Steiner et al. 2017, Adam et al. 2018).

To quantify the progress of recrystallization, grain average misorientation was used to define the recrystallized state of segments of cold-rolled and annealed U-10Mo microstructure. Previous authors have used similar metrics to diagnose the completion of recrystallization from EBSD maps (Malta et al. 2017, Division 2006, Dzaszyk et al. 2010). The kinetics of recrystallization for cold-rolled U-10Mo at 600°C and at 700°C as observed using this method are shown below in Figure 6.1.

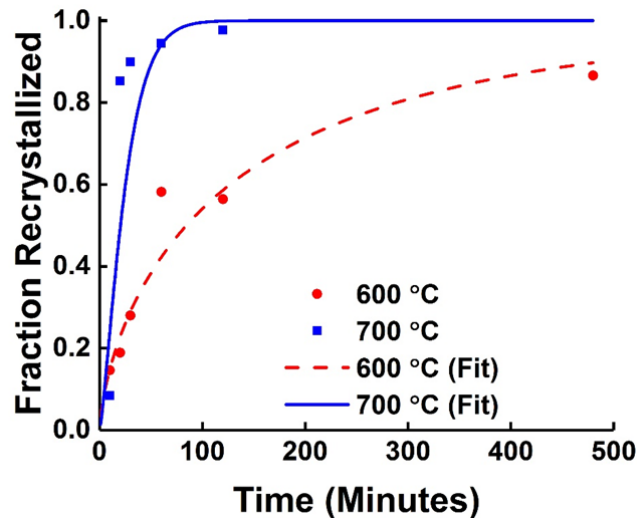


Figure 6.1. The Observed Recrystallization Progress of Cold-Rolled U-10Mo for 600°C and 700°C Anneals, Plotted Along with Their JMAK¹ Equation Fits

¹ JMAK is Johnson-Mehl-Avrami-Kolmogorov.

From these fits, we estimate a recrystallization activation energy of $100,596 \pm 23,070$ J/mol. This can be used as an input for recrystallization in simulations of annealing after both hot rolling, shown in Section 4.0, and cold rolling. This can be used to simulate recrystallization behavior after a cold roll, or combinations of hot rolling and cold rolling, as shown in Figure 6.2.

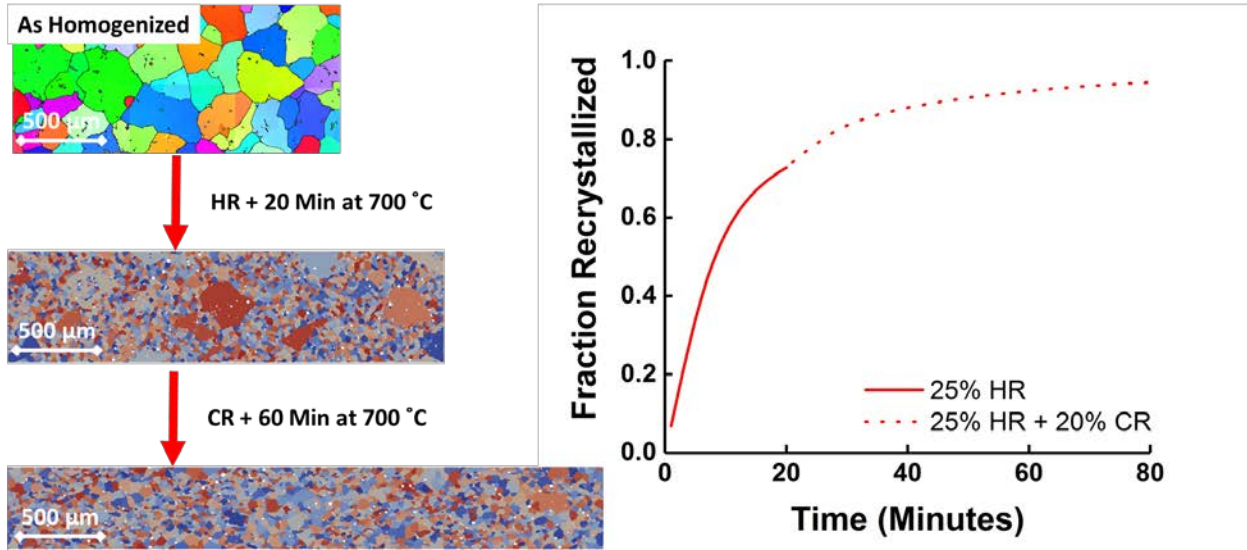


Figure 6.2. Grain Structure Evolution and Recrystallization Kinetics from an Integrated Simulation of Successive Hot Roll and Cold Roll of U-10Mo, with Intermediate Annealing Steps

6.2 Model Validation

Work validating this simulation work has not yet been performed.

6.3 Impact for Program

Our model has the capability to evaluate the deformation and recrystallization behavior for any combination of rolling and annealing treatment for hot rolling as well as cold rolling. This can be used to evaluate the differences between reduction through multiple passes and single rolling passes, as well as the differences between different hot-rolling and cold-rolling approaches, and provide an optimal rolling and annealing routine.

6.4 Tools Developed

This work extends the tools developed in Section 4.0 to analysis of microstructural evolution after cold rolling. Similar forms of analysis listed in Table 4.1 can be used to a similar effect for these segments of U-10Mo processing.

7.0 Post-Recrystallization Grain Growth

7.1 Model Description

After rolling and recrystallization, additional annealing is appropriate in order to promote a grain structure with features such as average grain diameter, morphology, and size distribution appropriate for service. These annealing treatments are expected to depend significantly on the attained microstructure from the previous homogenization, rolling, and annealing steps. For this purpose, a model of post-recrystallization grain growth was devised with which we can simulate grain structure evolution during this annealing treatment, which can last considerably longer than the intermediate anneals between rolling passes. Grain growth behavior is regularly described by the n -power law (Rollett et al. 2004, Thompson 1990, Abbaschian and Reed-Hill 1994, Beck et al. 1947, Schlenker et al. 2004), which follows the form

$$d^n - d_0^n = k_0 t e^{-Q_{Act}/RT} \quad (7.1)$$

Here, Q_{Act} is the activation energy of grain growth, k_0 is a constant, T is absolute temperature, and R is the universal gas constant. It is well known that Q_{Act} and k_0 can be obtained from fitting the observed grain growth coefficient k into an Arrhenius relationship with T . Actual behavior can deviate from this ideal case for multiple reasons, most notably the occurrence of grain boundary pinning (Yuksel and Ozkan 2015, Wang et al. 2013, Fasching et al. 1994) and solute dissolution (Liu et al. 2016, Gangulee and D'Huerle 1972). For this work, we assumed $n = 2$ for the first four hours of grain growth, and that the second phases present in the alloy remain inert between 700°C and 900°C. Figure 7.1 shows the temporal evolution of average grain sizes for 700°C, 800°C, and 900°C annealing treatments. U-10Mo grain growth kinetics increase dramatically with the increase of annealing temperature. The most rapid period of grain growth occurs in the first hour of annealing, followed by a period of stagnated grain growth. At 700°C, average grain diameter remains within the margin of error of the as-rolled and annealed material throughout the entire period.

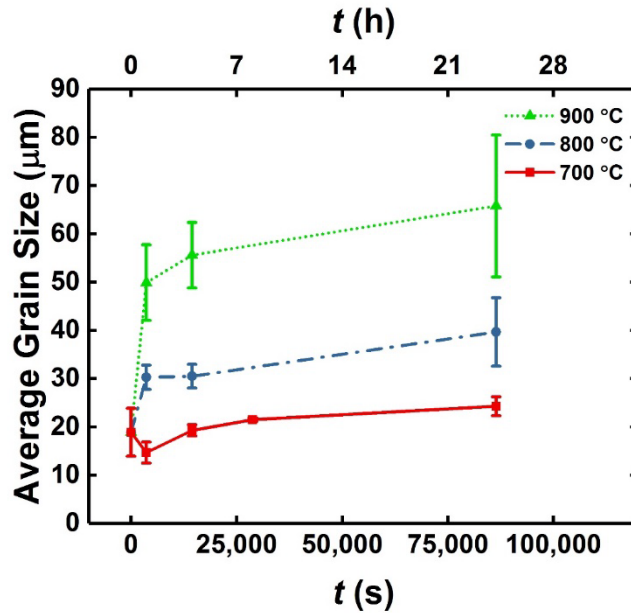


Figure 7.1. Average Grain Diameter of U-10Mo during Annealing at 700°C, 800°C, and 900°C. Grain growth follows a power-law relationship throughout the 24 h period of annealing.

To model this grain growth behavior, Potts model simulations were performed in microstructures reproduced by two BSE images of the U-10Mo samples, which were taken at magnifications of 250× and 150×. The resultant images had dimensions of 480 μm by 368 μm and 743 μm by 576 μm, respectively. The particles within the microstructure were segmented using ImageJ software (Schneider et al. 2012) and converted to 1280 × 957 and 1236 × 959 cell microstructures. The Potts model of grain growth was used to generate polycrystalline structures with an average grain size of 18.9 μm—the average diameter of the as-rolled and annealed microstructure—as determined from EBSD micrographs. The particle dispersions were then overlaid onto the polycrystalline structures.

The simulation temperature T_S was varied in these simulations to account for the changes in grain growth stagnation with temperature. Therefore, in order to quantify the effect of T_S on the simulated grain growth behavior, Potts model simulations were run on the starting microstructures for values of T_S ranging from 0.001 to 5.0, and the pinned grain size, the “Zener limit,” was approximated. The change in stagnation behavior is obvious from simulation micrographs. We show these for the captured particle dispersion at 250× in Figure 7.2.

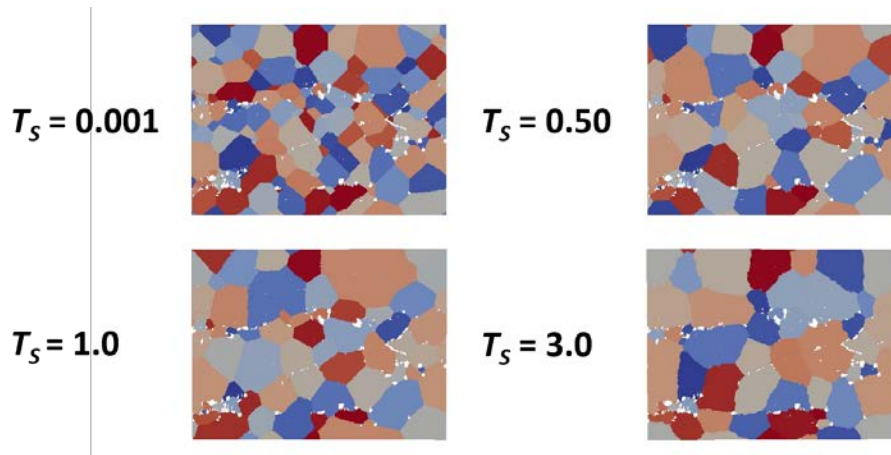


Figure 7.2. Stagnated Potts Model Microstructures Using Different Values of the Nonphysical Simulation Temperature T_S

7.2 Model Validation

Simulations were performed at temperatures of 700°C, 800°C, and 900°C for annealing periods of up to 240 h. The simulations performed at 700°C and 800°C were run using the 250× microstructure, while the simulation performed at 900°C was run on the 150× microstructure in order to obtain a wider field of view for the larger expected grain size. All of the model parameters used for the simulations described can be found in Table 7.1.

Table 7.1. Potts Model Simulation Parameters

Model Parameter	Value
l	0.375, 0.601 μm
T_S	0.001–4.072
Q	172.4 kJ
δ_0	7.66×10^{-6} (m^2/s)
T	973–1173 K (700–900°C)

The average grain size of U-10Mo in the Potts model can be seen in Figure 7.2, which also shows the experimental data obtained by Frazier et al. (2017) for comparison. From these plots it can be seen that while the Potts model slightly overestimates grain growth for 700°C and 800°C anneals, it underestimates grain size early in the 900°C anneal. A plot of the same data in comparison to the normal grain growth behavior predicted using the experimentally obtained activation energy of grain growth is shown in Figure 7.3.

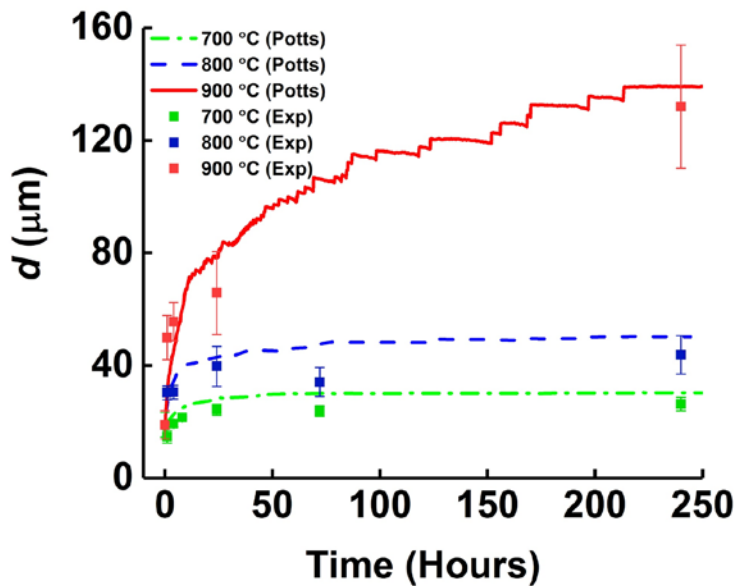


Figure 7.3. The Average Grain Size of U-10Mo as Predicted by the Potts Model , Assuming an Activation Energy for Grain Growth of 172.4 kJ/mole, Compared with the Experimentally Obtained Grain Growth Data

Our simulation approach suggests that smaller particles pin U-10Mo grain boundaries at lower temperatures, but that increasing temperature causes many of them to “escape” their pinned states at higher temperatures, until larger particles prevent further migration. The Potts model simulates this as random fluctuations of the grain boundaries. In this way, the mechanism resembles thermally activated grain boundary unpinning of nanoscale precipitates as suggested by Gore et al. (1989). The role of random fluctuations at positive T_S values in the Potts model has been previously documented (Sahni et al 1983, Harun et al. 2006, Miodownik et al. 1999) and random grain boundary fluctuations have previously been used to model grain growth behavior (Chen 1987, Louat 1974). However, it is unlikely that thermally activated unpinning is actually the cause of this observed grain growth in U-10Mo.

7.3 Impact for Program

Microstructure control is of clear interest to the program in order to control grain size and maintain acceptable spatial variations in grain size, both of which are known to affect fuel processing and performance under irradiation. Our method provides the program with a computational approach to determining the necessary post-rolling-and-annealing treatment for any given U-10Mo microstructure. Therefore, much of the cost of characterization to account for changes in processing parameters can be greatly reduced.

7.4 Tools Developed

Our method provides clear guidance for the post-recrystallization annealing of the LEU fuel. With this established model and a starting microstructure, our method can provide an annealing temperature and length of treatment that should attain the desired final microstructure with reasonable accuracy. In this way, the model of post-recrystallization can integrate with the previously described simulations of

homogenization, cold rolling, and annealing, in order to form a “closed loop” simulation of LEU processing.

8.0 Integration Framework

This section introduces the entire integration framework, from homogenization, hot rolling, annealing, to cold rolling, during U-10Mo fabrication, followed by the input and output variables for each individual process.

Starting from the homogenization process, a homogenization model is used to reconstruct a Mo concentration map for the entire microstructure domain based on the relationship between a BSE-SEM image and EDS line data. The homogenization model successfully captures the microstructure information during the homogenization evolution, which is valuable for studying U-10Mo for the subsequent processes. To produce uniform homogenization, a statistical method was proposed to quantify and characterize the Mo concentration variation in U-Mo fuel plates by analyzing the Mo concentration measurement data from SEM-EDS line scans. Statistical TIs were employed to determine the qualification of U-10Mo fuel plates.

An FEM model also was developed for deformation simulations using Mo concentration and carbide information from the homogenization model. The FEM model shows that Mo segregation leads to the nonuniform-thickness zirconium interlayer, and the nonuniformity can be largely alleviated by a complete homogenization process.

With initial second-phase particle distribution and morphology information given by the homogenization model, a carbide distribution analysis is performed to describe the distances and angles between particles during the rolling process from the material's initial state to the final reduced thickness. The probability distribution of particles serves as an indicator to determine interparticle spacing in the final rolling stages. With the new proposed stringer identification criterion, the evolution of SVF with rolling reduction was illustrated for different samples. Also, the maximum stringer length together with the near-surface particle distribution can be investigated. Results of that study would help determine optimized annealing process parameters for preparing U-10Mo samples with the desired microstructures for post-processing as well as the final fuel performance.

The progress in the development of an integrated simulation of U-10Mo alloy recrystallization during annealing has been described. The results show that the Potts model can integrate with mechanical deformation simulations to mimic the evolution of grain size. The developed recrystallization model should be capable of predicting recrystallization and grain growth behavior for any given processing history.

Plane-strain compression finite-element simulations were established for cold-rolling deformation with particle fracture considered. The obtained results, i.e., void volume fraction and fracture behaviors, are similar to the experimental observations. The results also demonstrated that the current simulation can accurately predict second-phase particle fracture during cold rolling.

The integrated model described in this report is an application of ICME technology. It shows potential applications of ICME to realistic modeling and analysis of the U-10Mo alloy. In the future, additional process models, including casting, carbon diffusion, HIP processing, and time-temperature transformation, will be developed to configure a complete ICME model of the U-10Mo alloy and output comprehensive microstructure predictions, such as phase stability, microstructural texture, grain growth, carbide morphology and fracture, porosity morphology, and eutectoid transformation.

In order to produce a fully functional integration model, the numerical modeling used in each step and the corresponding input/output files need to be clearly elucidated.

In the first step, homogenization, a BSE-SEM image with EDS line data from an as-cast U-10Mo sample is used as input. The homogenization model is implemented to reconstruct the Mo atomic concentration field from the given image. After that, the diffusion-based model can be used to predict homogeneity of Mo concentration at various homogenization times and temperatures. The output from this step provides a homogenized U-10Mo microstructure with Mo atomic or weight concentration distribution information, which will be used as input in the hot-rolling step. Note that the mapping of the Mo atomic concentration field from any U-10Mo sample at any homogenization time and temperature can be obtained from the homogenization model at this step.

The second step, hot rolling, consists of two models. The first model introduces the microstructure-based FEM modeling for U-10Mo/Zr interfacial structure prediction. By using the microstructural field generated from the homogenization model, the microstructure-based FEM is applied to study the effect of homogenization on the U-10Mo/Zr interaction during the rolling, especially the Zr thickness variation. The second model of this step performs a constant strain rate FEM simulation aiming to mimic the U-10Mo sample deformation via rolling and incorporate the carbide particle distribution analysis after the homogenization. With the given Mo concentration map, carbide distribution, and texture information from the homogenization model, the output from this FEM simulation can provide the deformation energy density and strain-stress information after each rolling cycle, which serves as input for the annealing process.

The macro-FEM hot-rolling model uses the U-10Mo and the can material temperature- and strain-rate-dependent mechanical properties as an input. The model is able to simulate multipass hot-rolling schedules with various reductions and roll speeds and predicts roll-separation force, torque, and possible foil defects during hot rolling. Model predictions, such as through-thickness strains, are used along with microstructural observations, such as recrystallization strain, to provide BWXT with an optimized rolling schedule.

The third step, recrystallization/annealing, employs the Potts model to predict the recrystallization kinetics, grain growth, and the effect of material processes on microstructures, which depends on the deformation information from the hot-rolling step. Note that the real-world U-10Mo processing involves multiple iterations of hot rolling and annealing. Thus, two-way information passing between hot rolling and annealing is required. More specifically, the deformation output from the FEM model will be supplied to the recrystallization model to simulate the microstructure evolution. Then the evolved microstructure from the recrystallization model will provide the texture information to the subsequent round of FEM modeling to calculate the deformation and stress/strain for the next round of recrystallization. Figure 8.1 shows an example of the integration between hot rolling and annealing. Starting from 0% reduction, as shown in Figure 8.1(a), the hot-rolling process is conducted to compress the sample until it has reached 40% reduction with a fixed strain rate (shown in Figure 8.1(b)). Then, the strain-stress information from FEM modeling is extracted and served as Potts model's input. After that, the sample undergoes a recrystallization cycle to provide the texture change and microstructure evolution. The detailed distribution of grains and carbide particles (highlighted in red) can be explicitly observed in Figure 8.1(c). Next, the sample undergoes hot-rolling treatment again and continues to be reduced to 65% using the microstructural information passed from the recrystallization cycle. In this example, the mechanical properties remain the same as those of 0% reduction for all the grains. Grain deformation and carbide particle (highlighted in red) distribution after this round of hot rolling are shown in Figure 8.1(d).

The iterative processes between hot rolling and annealing can be continued until a desired reduction percentage is achieved.

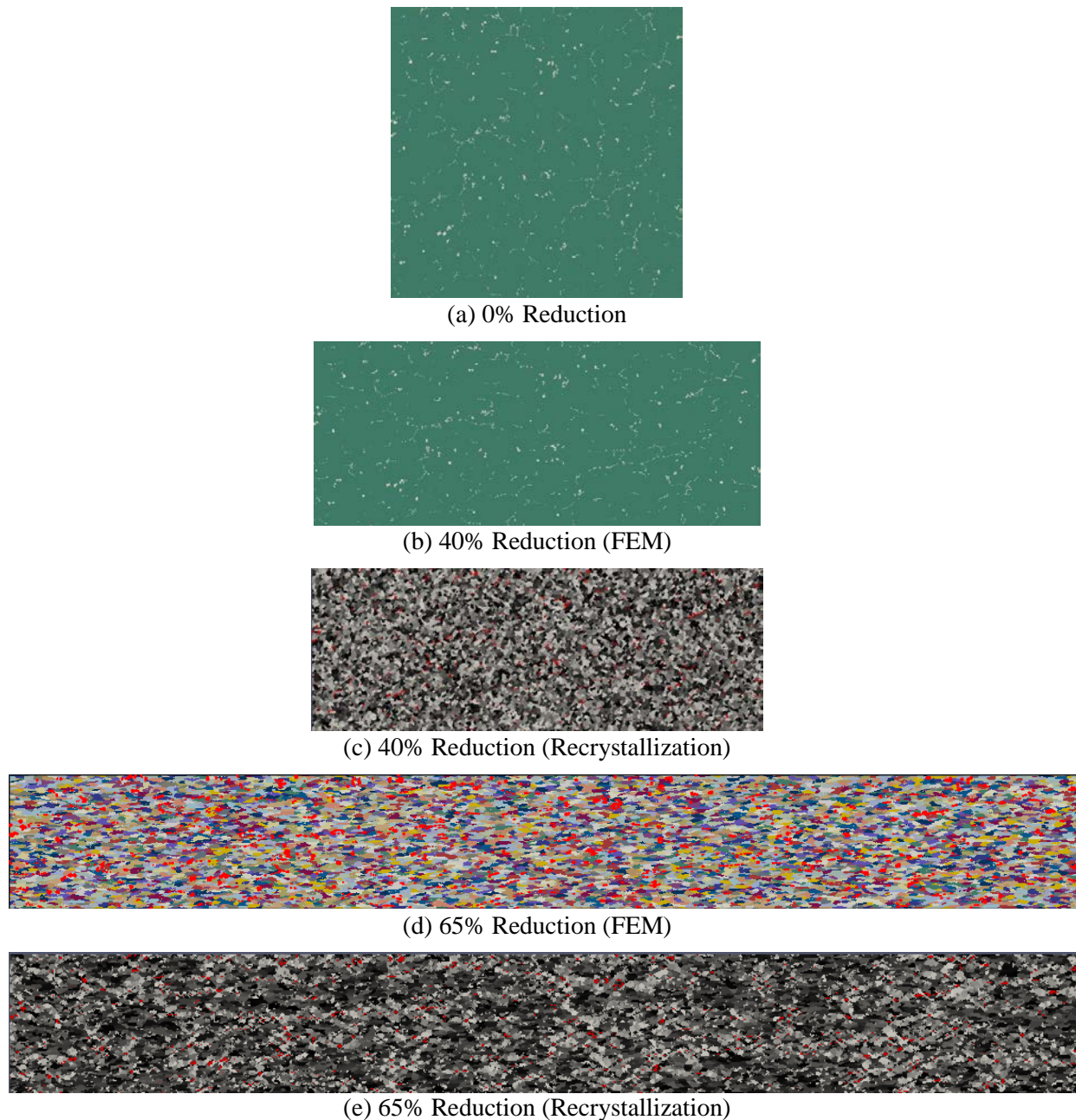


Figure 8.1. Integration between Hot Rolling and Recrystallization

The fourth step, cold rolling, uses a plane-strain FEM compression model in which microstructures containing particles obtained from optical microscopy are mapped from the previous step into the model for FEM. The cold-rolling simulation is performed with hard particle fracture considered. A tension failure criterion is attempted for the particle fracture; i.e., a particle will fracture after the hydrostatic tensile stresses of the particle reach a critical value.

The macro-cold-rolling FEM model uses U-10Mo mechanical properties at room temperature as an input to the model. The model predicts the roll-separation force and foil thickness as a function of roll diameter, roll speed, and tensioning. The model can suggest optimized rolling schedules with an optimized mill configuration.

9.0 References

- Abbaschian R and RE Reed-Hill. 1994. *Physical Metallurgy Principles*. CL Engineering, 3rd Edition.
- Adam K, D Zöllner, DP Field. 2018. “3D microstructural evolution of primary recrystallization and grain growth in cold rolled single-phase aluminum alloys.” *Modelling and Simulation in Materials Science and Engineering* 27 February 2018. DOI: 10.1088/1361-651X/aaa146.
- Allison J, D Backman, and L Christodoulou. 2006a. “Integrated computational materials engineering: a new paradigm for the global materials profession.” *Journal of The Minerals* 58(11):25–7.
- Allison J, M Li, C Wolverton, and X Su. 2006b. “Virtual aluminum castings: an industrial application of ICME.” *Journal of The Minerals* 58(11):28–35.
- ASTM E45-05. 2005. *Standard Test Methods for Determining the Inclusion Content of Steel*. ASTM International, West Conshohocken, PA. www.astm.org.
- Backman DG, DY Wei, DD Whitis MB Buczek PM Finnigan, and D Gao. 2006. “ICME at GE: accelerating the insertion of new materials and processes.” *Journal of The Minerals* 58(11):36–41.
- Beck PA, JC Kremer, LJ Demer, and ML Holzworth. 1947. “Grain Growth in High-Purity Aluminum and in an Aluminum-Magnesium Alloy.” *Trans. AIME* 175(948):372.
- Beghi G. 1968. *Gamma Phase Uranium-Molybdenum Fuel Alloys*. European Atomic Energy Community, Joint Nuclear Research Center, Ispra Establishment (Italy).
- Beynon JH, and CM Sellars. 1992. “Modelling microstructure and its effects during multipass hot rolling.” *ISIJ International* 32(3):359–367.
- Bostrom W and E Halteman. 1956. *The Metastable Gamma Phase in Uranium Base Molybdenum Alloys*. Westinghouse Electric Corp., Pittsburgh, PA.
- Burkes DE, T Hartmann, R Prabhakaran, and J F Jue. 2009a. “Microstructural characteristics of DU-xMo alloys with $x = 7-12$ wt%.” *Journal of Alloys and Compounds* 479(1–2):140–147.
- Burkes DE, R Prabhakaran, J F Jue, and FJ Rice. 2009b. “Mechanical properties of DU-xMo alloys with $x = 7$ to 12 weight percent.” *Metallurgical and Materials Transactions A* 40(5):1069–1079.
- Burkes DE, R Prabhakaran, T Hartmann, J-F Jue, and FJ Rice. 2010. “Properties of DU–10wt% Mo alloys subjected to various post-rolling heat treatments.” *Nuclear Engineering and Design* 240(6):1332–1339.
- Butcher B and B Hatt. 1964. “The mechanical properties of quenched uranium-molybdenum alloys: part II: a preliminary survey of the deformation mechanisms.” *Journal of Nuclear Materials* 11(2):163–182.
- Cahn JW. 1962. “The impurity-drag effect in grain boundary motion.” *Acta Metallurgica* 10:789–98. DOI: 10.1016/0001-6160(62)90092-5.
- Cao W, S-L Chen, F Zhang, K Wu, Y Yang, Y Chang, R Schmid-Fetzer, and W Oats. 2009. “PANDAT software with PanEngine, PanOptimizer and PanPrecipitation for multi-component phase diagram calculation and materials property simulation.” *CALPHAD* 33(2):328–342.
- Chen I. 1987. “A Stochastic Theory of Grain Growth.” *Acta Metallurgica* 35:1723–1733.
- Cheng G, EI Barker, EV Stephens, KS Choi, and X Sun. 2016a. “Quantifying grain level stress-strain behavior for AM40 via instrumented microindentation.” *MRS Advances* 1(12):761–772.
- Cheng G, KS Choi, X Hu, and X Sun. 2016b. “Determining individual phase properties in a multi-phase Q&P steel using multi-scale indentation tests.” *Materials Science and Engineering A* 652:384–95.

- Cheng G, X Hu, WE Frazier, CA Lavender, and VV Joshi. 2018. “Effect of second phase particles and stringers on microstructures after rolling and recrystallization.” *Materials Science and Engineering A* 736:41–52. DOI: 10.1016/j.msea.2018.08.040.
- Choi K., C. Wang, C.A. Lavender, and V.V. Joshi. 2018. *Carbide Particle Redistribution in U10Mo Alloy during Hot Rolling Process*. PNNL-28383. Pacific Northwest National Laboratory, Richland, WA.
- Craik R, D Birch, C Fizzotti, and F Saraceno. 1962. “Phase equilibria in uranium-rich binary alloys containing molybdenum and zirconium and the effect of ternary additions of carbon.” *Journal of Nuclear Materials* 6(1):13–25.
- Crapps J, Clarke K, Katz J, Alexander DJ, Aikin B, Vargas VD, JD Montalvo, DE Dombrowski, and B Mihaila. 2013. “Development of the hot isostatic press manufacturing process for monolithic nuclear fuel.” *Journal of The Minerals, Metals & Materials Society* 254:43–52.
- Daigne J, M Guttman, and J Naylor. 1982. “The influence of lath boundaries and carbide distribution on the yield strength of 0.4% C tempered martensitic steels.” *Materials Science and Engineering* 56(1):1–10.
- DeMint AL, JG Gooch, KR Crane, and DE Fleury. 2013. *Uranium-10% Molybdenum Parametric Study 1: Alloying*. Y/DV 2272, Rev. 1, Y-12 National Security Complex, Oak Ridge, TN.
- Devaraj A, VV Joshi, S Jana, L Sweet, C Mcinnis, S Manandhar, and CA Lavender. 2016a. *Detecting the Extent of Eutectoid Transformation in U-10Mo*. PNNL-SA-120714, Pacific Northwest National Laboratory, Richland, WA.
- Devaraj A, L Kovarik, VV Joshi, S Jana, S Manandhar, BW Arey, and CA Lavender. 2016b. *High-Resolution Characterization of UMo Alloy Microstructure*. PNNL-26020. Pacific Northwest National Laboratory, Richland, WA.
- Devaraj A, R Prabhakaran, VV Joshi, SY Hu, E McGarrah, and CA Lavender. 2016c. *Theoretical Model for Volume Fraction of UC, ²³⁵U Enrichment, and Effective Density of Final U-10Mo Alloy*. PNNL-SA-117284, Pacific Northwest National Laboratory, Richland, WA.
- Devaraj A, L Kovarik, CA Lavender, EJ Kautz EJ, and VV Joshi. 2017. *Effect of Silicon in U-10Mo Alloy*. PNNL-26790, Pacific Northwest National Laboratory, Richland, WA.
- Division T. 2006. “Analysis of recrystallized volume fractions in uranium using electron backscatter diffraction.” *Journal of Microscopy* 223:33–39. DOI: 10.1111/j.1365-2818.2006.01595.x
- Dziaszyk S, EJ Payton, F Friedel, V Marx, G Eggeler. 2010. “On the characterization of recrystallized fraction using electron backscatter diffraction: A direct comparison to local hardness in an IF steel using nanoindentation.” *Mater. Sci. Eng. A* 527:7854–7864. DOI: 10.1016/j.msea.2010.08.063.
- Edwards DJ, RM Ermi, AL Schemer-Kohn, NR Overman, CH Henager Jr., D Burkes, and DJ Senior. 2012. *Characterization of U-Mo Foils for AFIP-7*. PNNL-21990. Pacific Northwest National Laboratory, Richland, WA.
- Fasching AA, GR Edwards, SA David. 1994. “Grain Growth Kinetics of an Iron Aluminide Alloy.” *Scr. Metall. Mater.* 30:1003–1008.
- Frazier WE, GS Rohrer, and AD Rollett. 2015. “Abnormal grain growth in the Potts model incorporating grain boundary complexion transitions that increase the mobility of individual boundaries.” *Acta Metallurgica* 96:390–398.
- Frazier WE, S Hu, N Overman, C Lavender, and VV Joshi. 2018. “Short Communication on Kinetics of Grain Growth and Particle Pinning in U-10 wt% Mo.” *J. Nucl. Mater.* 498:254–258.

- Fujiyama N, T Nishibata, A Seki, H Hirata, K Kojima, and K Ogawa. 2017. “Austenite grain growth simulation considering the solute-drag effect and pinning effect.” *Science and Technology of Advanced Materials* 18:88–95. DOI: 10.1080/14686996.2016.1244473.
- Gangulee A, FM D’Heurle. 1972. “Anomalous large grains in alloyed aluminum thin films I. Secondary grain growth in aluminum-copper films.” *Thin Solid Films* 12:399–402. DOI: 10.1016/0040-6090(72)90103-4.
- Garde AM, HM Chung, and TF Kassner. 1977. *Uniaxial Tensile Properties of Zircaloy Containing Oxygen: Summary Report*. ANL 77–30, Argonne National Laboratory, Argonne, Illinois.
- Gates JE, EG Bodine, JC Bell, AA Bauer, and GD Calkins. 1958. *Stress-Strain Properties of Irradiated Uranium-10 w/o Molybdenum*. BMI-APDA-638, Battelle Memorial Institute, Columbus, OH.
- Gore MJ, M Grujicic, GB Olson, and M Cohen. 1989. “Thermally activated grain boundary unpinning.” *Acta Metallurgica* 37:2849–2854. DOI: 10.1016/0001-6160(89)90320-9.
- Hannard F, S Castin, E Maire, R Mokso, T Pardoën, and A Simar. 2017. “Ductilization of aluminum alloy 6056 by friction stir processing.” *Acta Metallurgica* 130:121–36.
- Harun A, EA Holm, MP Clode, and MA Miodownik. 2006. “On computer simulation methods to model Zener pinning.” *Acta Metallurgica* 54:3261–3273. DOI: 10.1016/j.actamat.2006.03.012.
- Helle A, KE Easterling, and M Ashby. 1985. “Hot-isostatic pressing diagrams: new developments.” *Acta Metallurgica* 33(12):2163–2174.
- Henager CHJ, WD Bennett, AL Doherty, ES Fuller, JS Hardy, and RP Omberg. 2014. *Corrosion Report for the U-Mo Fuel Concept*. PNNL-23592, Pacific Northwest National Laboratory, Richland, WA.
- Higgins GT. 1974. “Grain-boundary migration and grain growth.” *Metal Science* 8:143–150. DOI: 10.1179/msc.1974.8.1.143.
- Hills R, B Butcher, and B Howlett. 1964. “The mechanical properties of quenched uranium-molybdenum alloys: part I: tensile tests on polycrystalline specimens.” *Journal of Nuclear Materials* 11(2):149–162.
- Hoge K. 1966. “Some mechanical properties of U–10% Mo alloy under dynamic tension loads.” *Journal of Basic Engineering* 6:509–517.
- Holm EA, MA Miodownik, and AD Rollett. 2003. “On abnormal subgrain growth and the origin of recrystallization nuclei.” *Acta Metallurgica* 51(9):2701–2716.
- Holm EA, TD Hoffmann, AD Rollett, and CG Roberts. 2015. “Particle-assisted abnormal grain growth.” *IOP Conference Series: Materials Science* 2015:89.
- Hu SY, Joshi VV, Lavender CA, Lombardo NJ, Wight J, Ye B, et al. 2016. *Microstructural level fuel performance modeling of UMo monolithic fuel*. INL/LTD-16-40028, Idaho National Laboratory, Idaho Falls, ID. (Limited Distribution)
- Hu XH, M Jain, D Wilkinson, and RK Mishra. 2008. “Microstructure-based finite element analysis of strain localization behavior in AA5754 aluminum sheet.” *Acta Metallurgica* 56(13):3187–3201.
- Hu X, X Wang, VV Joshi, and CA Lavender. 2018. “The effect of thermomechanical processing on second phase particle redistribution in U-10wt%Mo.” *Journal of Nuclear Materials* 500:270–279. DOI: 10.1016/j.jnucmat.2017.12.042.
- INL – Idaho National Laboratory. 2017. *Fuel Specification for MP-1, MP-2, and FSP-1*. SPC 1691, Idaho National Laboratory, Idaho Falls, Idaho.

- Jana S, VV Joshi, A Devaraj, L Kovarik, LE Sweet, S Manandhar, T Varga, and CA Lavender. *Phase Transformation Kinetics in a U-10wt%Mo Cast, Homogenized Alloy at 500°C and 400°C*. PNNL-25990, Pacific Northwest National Laboratory, Richland, WA.
- Joost WJ. 2012. “Reducing vehicle weight and improving U.S. energy efficiency using integrated computational materials engineering.” *Journal of The Minerals* 64(9):1032–1038.
- Joshi VV, EA Nyberg, CA Lavender, D Paxton, and DE Burkes. 2015a. “Thermomechanical process optimization of U-10wt% Mo–Part 2: The effect of homogenization on the mechanical properties and microstructure.” *Journal of Nuclear Materials* 465:710–718.
- Joshi VV, EA Nyberg, CA Lavender, D Paxton, H Garmestani, and DE Burkes. 2015b. “Thermomechanical process optimization of U-10wt% Mo–Part 1: high-temperature compressive properties and microstructure.” *Journal of Nuclear Materials*. 465(2015):805–813.
- Joshi VV, DM Paxton, CA Lavender, and D Burkes. 2016. *The Effect of Rolling As-Cast and Homogenized U-10Mo Samples on the Microstructure Development and Recovery Curves*. PNNL-25781, Pacific Northwest National Laboratory, Richland, WA.
- Kautz EJ, A Devaraj, L Kovarik, CA Lavender, and VV Joshi. 2017a. *Effect of Silicon in U-10Mo Alloy*. PNNL-26790, Pacific Northwest National Laboratory, Richland, WA.
- Kautz EJ, S Jana, A Devaraj, CA Lavender, LE Sweet, and VV Joshi. 2017b. *Detecting the Extent of Cellular Decomposition after Sub-Eutectoid Annealing in Rolled UMo Foils*. PNNL-26862, Pacific Northwest National Laboratory, Richland, WA.
- Li D and C Lavender. 2015. “Strengthening and improving yield asymmetry of magnesium alloys by second phase particle refinement under the guidance of integrated computational materials engineering.” *Journal of Engineering Materials and Technology–Transactions of the ASME* 137(3):031008.
- Liu M, W Zheng, J Xiang, Z Song, E Pu, and H Feng. 2016. “Grain Growth Behavior of Inconel 625 Superalloy.” *Journal of Iron Steel Research International* 23:1111–1118. DOI: 110.1016/S1006-706X(16)30164-9.
- Liu M, W Zheng, J Xiang, Z Song, E Pu, H Feng. 2016. “Grain Growth Behavior of Inconel 625 Superalloy.” *J. Iron Steel Res. Int.* 23:1111–1118. DOI: 10.1016/S1006-706X(16)30164-9.
- Llorca J, C González, JM Molina-Aldareguía, J Segurado, R Seltzer, F Sket, M Rodríguez, S Sádaba, R Muñoz, and LP Canal. 2011. “Multiscale modeling of composite materials: a roadmap towards virtual testing.” *Advanced Materials* 23(44):5130–5147.
- Louat NP. 1974. “On the Theory of Normal Grain Growth.” *Acta Metallurgica* 22:721–724.
- Malta PO, DS Alves, AOV Ferreira, ID Moutinho, CAP Dias, DB Santos. 2017. “Static Recrystallization Kinetics and Crystallographic Texture of Nb-Stabilized Ferritic Stainless Steel Based on Orientation Imaging Microscopy.” *Metall. Mater. Trans. A – Phys. Metall. Mater. Sci.* 48:1288–1309. DOI: 10.1007/s11661-016-3935-3.
- Meurling F, A Melander, M Tidesten, and L Westin. 2001. “Influence of carbide and inclusion contents on the fatigue properties of high speed steels and tool steels.” *International Journal of Fatigue* 23(3):215–224.
- Meyer M, G Hofman, S Hayes, C Clark, T Wiencek, J Snelgrove, RV Strain, and K-H Kim. 2002. “Low-temperature irradiation behavior of uranium-molybdenum alloy dispersion fuel.” *Journal of Nuclear Materials* 304(2):221–236.
- Miller GK, DE Burkes, and DM Wachs. 2010. “Modeling thermal and stress behavior of the fuel-clad interface in monolithic fuel mini-plates.” *Materials & Design* 31(7):3234–3243.

- Miodownik M, JW Martin, and A Cerezo. 1999. “Mesoscale simulations of particle pinning.” *Philosophical Magazine A* 79:203–222. DOI: 10.1080/01418619908214284.
- MJ Gore, M Grujicic, GB Olson, M Cohen. 1989. “Thermally activated grain boundary unpinning.” *Acta Metall.* 37:2849–2854. DOI: 10.1016/0001-6160(89)90320-9.
- Moore IJ, JI Taylor, MW Tracy, MG Burke, and EJ Palmiere. 2017. “Grain coarsening behaviour of solution annealed Alloy 625 between 600–800°C.” *Materials Science and Engineering: A* 682:402–409. DOI: 10.1016/j.msea.2016.11.060.
- NP Louat. 1974. “On the Theory of Normal Grain Growth.” *Acta Metall.* 22:721.
- Nyberg EA, DE Burkes, VV Joshi, and CA Lavender. 2015. *The Microstructure of Rolled Plates from Cast Billets of U-10Mo Alloys*. PNNL-24160, Pacific Northwest National Laboratory, Richland, WA.
- Nyberg EA, VV Joshi, CA Lavender, and D Burkes. 2012. *Summary of Compression Testing of U-10Mo*. PNNL-21932, Pacific Northwest National Laboratory, Richland, WA.
- Nyberg EA, VV Joshi, CA Lavender, DM Paxton, and DE Burkes. 2013. *The Influence of Casting Conditions on the Microstructure of As-Cast U-10Mo Alloys: Characterization of the Casting Process Baseline*. PNNL-23049, Pacific Northwest National Laboratory, Richland, WA.
- Nyberg EA, VV Joshi, CA Lavender, DM Paxton, and DE Burkes. 2014. *Influence of Homogenization on the Mechanical Properties and Microstructure of the U-10Mo Alloy*. PNNL-23348, Pacific Northwest National Laboratory, Richland, WA.
- Ozaltun H, M-HH Shen, and P Medvedev. 2011. “Assessment of residual stresses on U10Mo alloy based monolithic mini-plates during Hot Isostatic Pressing.” *Journal of Nuclear Materials* 419(1):76–84.
- Ozaltun H, M-HH Shen, P Medvedev, and SJ Miller. 2013. “Computational evaluation for the mechanical behavior of U10Mo fuel mini plates subject to thermal cycling.” *Nuclear Engineering and Design* 254:165–178.
- Panchal JH, SR Kalidindi, and DL McDowell. 2013. “Key computational modeling issues in integrated computational materials engineering.” *Computer-Aided Design* 45(1):4–25.
- Park CS, TW Na, HK Park, BJ Lee, CH Han, and NM Hwang. 2012. “Three-dimensional Monte Carlo simulation for the effect of precipitates and sub-boundaries on abnormal grain growth.” *Scripta Materialia* 66(6):398–401.
- Pietrzyk M and J Lenard. 2012. *Thermal-Mechanical Modelling of the Flat Rolling Process*. Springer Science & Business Media.
- Potts RB and JC Ward. 1955. “The combinatorial method and the 2-dimensional Ising model.” *Progress of Theoretical Physics* 13(1):38–46. DOI: 10.1143/PTP.13.38.
- Prabhakaran R, A Devaraj, VV Joshi, and CA Lavender. 2016a. *Procedure for Uranium-Molybdenum Density Measurements and Porosity Determination*. PNNL-25793, Pacific Northwest National Laboratory, Richland, WA.
- Prabhakaran R, VV Joshi, A Devaraj, and CA Lavender. 2017. *Three-Point Bend Testing of Unirradiated U-Mo Fuel Foils*. PNNL-26662, Pacific Northwest National Laboratory, Richland, WA.
- Prabhakaran R, VV Joshi, MA Rhodes, AL Schemer-Kohrn, AD Guzman, and CA Lavender. 2016b. *U-10Mo Sample Preparation and Examination using Optical and Scanning Electron Microscopy*. PNNL-25308, Rev. 1, Pacific Northwest National Laboratory, Richland, WA.
- Raabe D. 2000. “Scaling Monte Carlo kinetics of the Potts model using rate theory.” *Acta Metallurgica* 48(7):1617–1628.

- Rahmohan YHN and JA Szpunar. 1998. “Monte Carlo Simulation on the Abnormal Growth of Goss Grains in Fe 3% Si Conventional Steel.” *Proceedings Third International Conference on Grain Growth, ICGG-3*, June 14–19, 1998, Carnegie Mellon University, Pittsburgh, PA.
- Rollett AD, DJ Srolovitz, and MP Anderson. 1989. “Simulation and theory of abnormal grain-growth anisotropic grain-boundary energies and mobilities.” *Acta Metallurgica* 37(4):1227–1240.
- Rollett AD, DJ Srolovitz, MP Anderson, and RD Doherty. 1992. “Computer-simulation of recrystallization –III. Influence of a dispersion of fine particles.” *Acta Metallurgica* 40(12):3475–3495.
- Rollett AD, G Gottstein, LS Shvindlerman, DA Molodov. 2004. “Grain boundary mobility – a brief review.” *Zeitschrift Fur Met.* 95:226–229. DOI: 10.3139/146.017938.
- Safran S, PS Sahni, and GS Grest. 1983. “Kinetics of ordering in two dimensions. I. Model systems.” *Physical Review B* 28(5):2693–2704. DOI: 10.1103/PhysRevB.28.2693.
- Sahni PS, DJ Srolovitz, GS Grest, MP Anderson, and SA Safran. 1983. “Kinetics of ordering in two dimensions. II. Quenched systems.” *Physical Review B* 28:2705–2716. DOI: 10.1103/PhysRevB.28.2705.
- Schlenker T, ML Valero, HW Schock, JH Werner. 2004. “Grain growth studies of thin Cu(In, Ga)Se₂ films.” *J. Cryst. Growth.* 264:178–183. DOI: 10.1016/j.jcrysgro.2004.01.020.
- Schneider CA, WS Rasband, and KW Eliceiri. 2012. “NIH Image to ImageJ: 25 years of image analysis.” *Nature Methods* 9(2012):671–675. DOI: 10.1038/nmeth.2089.
- Sease J, R Primm III, and J Miller. 2007. *Conceptual process for the manufacture of low-enriched uranium/molybdenum fuel for the high flux isotope reactor*. ORNL/TM 2007/39, Oak Ridge National Laboratory, Oak Ridge, TN. DOI: 10.2172/921766.
- Senor DJ and DE Burkes. 2014. *Fuel Fabrication Capability Research and Development Plan*. PNNL-22528, Rev. 1, Pacific Northwest National Laboratory, Richland, WA.
- Snelgrove JL, G Hofman, M Meyer, C Trybus, and T Wiencek. 1997. “Development of very-high-density low-enriched-uranium fuels.” *Nuclear Engineering and Design* 178(1):119–126.
- Soulami A, C Lavender, D Paxton, and D Burkes. 2014. *Rolling Process Modeling Report: Finite-Element Prediction of Roll-Separating Force and Rolling Defects*. PNNL-23313, Pacific Northwest National Laboratory, Richland, WA.
- Soulami A, C Lavender, D Paxton, and D Burkes. 2015. *Rolling Process Modeling Report: Finite-Element Model Validation and Parametric Study on Various Rolling Process Parameters*. PNNL-24362, Pacific Northwest National Laboratory, Richland, WA.
- Soulami A, Z Xu, VV Joshi, D Burkes, C Lavender, and E McGarrah. 2016. *U-10Mo/Zr Interface Modeling using a Microstructure-Based FEM Approach*. PNNL-25365, Pacific Northwest National Laboratory; Richland, WA.
- Soulami A, DE Burkes, VV Joshi, CA Lavender, and D Paxton. 2017. “Finite-element model to predict roll-separation force and defects during rolling of U-10Mo alloys.” *Journal of Nuclear Materials* 494(Supplement C):182–191.
- Steiner MA, RJ McCabe, E Garlea, SR Agnew. 2017. “Monte Carlo modeling of recrystallization processes in α -uranium.” *J. Nucl. Mater.* 492:74–87. DOI: 10.1016/j.jnucmat.2017.04.026.
- Thomas BG. 2002. “Modeling of the continuous casting of steel—past, present, and future.” *Metallurgical and Materials Transactions B* 33(6):795–812.
- Thompson CV. 1990. “Grain Growth in Thin Films.” *Annu. Rev. Mater. Sci.* 20:245–268.

- Tikare V and EA Holm EA. 1998. "Simulation of grain growth and pore migration in a thermal gradient." *Journal of the American Ceramic Society* 81(3):480–484.
- Tikare V and JD Cawley. 1998a. "Application of the Potts model to simulation of Ostwald ripening." *Journal of the American Ceramic Society* 81(3):485–491.
- Tikare V and JD Cawley. 1998b. "Numerical simulation of grain growth in liquid phase sintered materials - I. Model." *Acta Metallurgica* 46(4):1333–1342.
- Torquato S. 2013. *Random Heterogeneous Materials: Microstructure and Macroscopic Properties*. Springer Science & Business Media. Berlin, Germany.
- Wachs DM, CR Clark, and RJ Dunavant. 2008. *Conceptual Process Description for the Manufacture of Low-Enriched Uranium-Molybdenum Fuel*. INL/EXT-08-13840, Idaho National Laboratory, Idaho Falls, ID.
- Waldron M, R Burnett, and S Pugh. 1958. *The Mechanical Properties of Uranium-Molybdenum Alloys*. United Kingdom Atomic Energy Authority. Research Group. Atomic Energy Research Establishment, Harwell, Berkshire, England.
- Wang C., Z. Xu, D.K. Fagan, D.P. Field, C.A. Lavender, and V.V. Joshi. 2019. *Quantifying and Qualifying Alloys Based on Level of Homogenization: A U 10 wt% Mo Alloy Case Study*. PNNL-28495. Pacific Northwest National Laboratory, Richland, WA.
- Wang K, MQ Li, C Li. 2013. "Delta and Austenite Phases Evolution and Model in Solution Treatment of Superalloy GH4169." *Mater. Sci. Technol.* 29:346–350.
- Wang X, Z Xu, A Soulami, X Hu, C Lavender, and V Joshi. 2017. "Modeling Early-Stage Processes of U-10 Wt% Mo Alloy Using Integrated Computational Materials Engineering Concepts", *JOM* 69(12): 2532-2537.
- Williamson A and JP Delplanque. 2016. "Investigation of dynamic abnormal grain growth using the Monte Carlo Potts method." *Computational Materials Science* 124:114–129.
- Xu Z, V Joshi, S Hu, D Paxton, C Lavender, and D Burkes. 2016. "Modeling the homogenization kinetics of as-cast U-10wt% Mo alloys." *Journal of Nuclear Materials* 471:154–164.
- Yuksel B and TO Ozkan. 2015. "Grain growth kinetics for B₂O₃-doped ZnO ceramics." *Materials Science–Poland* 33(2):220–229. DOI: 10.1515/msp-2015-0029.
- Zöllner D. 2014. "A new point of view to determine the simulation temperature for the Potts model simulation of grain growth." *Computational Materials Science* 86:99–107. DOI: 10.1016/j.commatsci.2014.01.044.



Pacific Northwest
NATIONAL LABORATORY

*Proudly Operated by **Battelle** Since 1965*

902 Battelle Boulevard
P.O. Box 999
Richland, WA 99352
1-888-375-PNNL (7665)

U.S. DEPARTMENT OF
ENERGY

www.pnnl.gov